

## ELLERMAN BOMBS AT HIGH RESOLUTION III. SIMULTANEOUS OBSERVATIONS WITH IRIS AND SST

G. J. M. VISSERS<sup>1</sup>, L. H. M. ROUPPE VAN DER VOORT<sup>1</sup>, R. J. RUTTEN<sup>2,1</sup>, M. CARLSSON<sup>1</sup>, AND B. DE PONTIEU<sup>3,1</sup><sup>1</sup>Institute of Theoretical Astrophysics, University of Oslo, P.O. Box 1029 Blindern, N-0315 Oslo, Norway; g.j.m.vissers@astro.uio.no<sup>2</sup>Lingezicht Astrophysics, 't Oosteneind 9, 4158CA Deil, The Netherlands and<sup>3</sup>Lockheed Martin Solar and Astrophysics Laboratory, 3251 Hanover Street, Org. A021S, Bldg. 252, Palo Alto, CA 94304, USA*Draft version Friday 3<sup>rd</sup> July, 2015*

## ABSTRACT

Ellerman bombs are transient brightenings of the extended wings of the solar Balmer lines in emerging active regions. We describe their properties in the ultraviolet lines sampled by the Interface Region Imaging Spectrograph (IRIS), using simultaneous imaging spectroscopy in  $H\alpha$  with the Swedish 1-m Solar Telescope (SST) and ultraviolet images from the Solar Dynamics Observatory for Ellerman bomb detection and identification. We select multiple co-observed Ellerman bombs for detailed analysis. The IRIS spectra strengthen the view that Ellerman bombs mark reconnection between bipolar kilogauss fluxtubes with the reconnection and the resulting bi-directional jet located within the solar photosphere and shielded by overlying chromospheric fibrils in the cores of strong lines. The spectra suggest that the reconnecting photospheric gas underneath is heated sufficiently to momentarily reach stages of ionization normally assigned to the transition region and the corona. We also analyze similar outburst phenomena that we classify as small flaring arch filaments and ascribe to higher-located reconnection. They have different morphology and produce hot arches in million-Kelvin diagnostics.

*Subject headings:* Sun: activity – Sun: atmosphere – Sun: magnetic fields

## 1. INTRODUCTION

Ellerman (1917) discovered intense short-lived brightenings of the extended wings of the Balmer  $H\alpha$  line at 6563 Å that he called “solar hydrogen bombs”. They are called Ellerman bombs (henceforth EB) since McMath et al. (1960). For more detail we refer to the excellent summary by Georgoulis et al. (2002) and our more recent review of the extensive EB literature in Rutten et al. (2013).

We discuss the subsequent EB literature below, but here point out the recent discovery by Peter et al. (2014) of very hot “bombs” in ultraviolet spectra from the Interface Region Imaging Spectrograph (IRIS, De Pontieu et al. 2014). The present paper addresses their suggestion that these bombs might have been EBs or similar to EBs.

A major motivation to study EBs is that they supposedly mark locations of serpentine flux rope emergence in newly emerging active regions (e.g., Bernasconi et al. 2002; Pariat et al. 2004; Isobe et al. 2007; Archontis & Hood 2009; Pariat et al. 2009). Understanding their nature may therefore present a way to measure active region evolution, in particular the reconnective field topology evolution that eventually produces much larger solar outbursts. In this context, EBs should become useful as telltales of strong-field reconnection when well understood.

In addition, the complex physics and spectrum formation of the EB phenomenon are of interest per sé since EBs appear to be pockets of hot gas within the photosphere. The discovery of extremely hot IRIS bombs by Peter et al. (2014) that also appear to be photospheric enhances this interest. In our present series of EB analyses we employ high-quality imaging spectroscopy with the Swedish 1-m Solar Telescope (SST; Scharmer et al. 2003) to study EBs at unprecedented spatial, spectral, and temporal resolution. Paper I (Watanabe et al. 2011) established that EBs are a purely photospheric

phenomenon.

Paper II (Vissers et al. 2013) added evidence that EBs mark magnetic reconnection of strong opposite-polarity field concentrations in the low photosphere and discussed their appearance in 1700 Å images from the Atmospheric Imaging Assembly (AIA; Lemen et al. 2012) of the Solar Dynamics Observatory (SDO).

Let us morphologically define the three bomb-like phenomena that we discuss below, based on our inspections of dozens of such features in SST, SDO, and IRIS data. More detail on their recognition is given in Sect. 2.

We define “Ellerman bombs” (EB) as substantial brightenings of the extended wings of  $H\alpha$  without core brightening that, at sufficient angular and temporal resolution, show definite rapid-flame morphology when viewed from aside as described in Paper I. EB  $H\alpha$  wing brightenings exceed those from much more ubiquitous magnetic concentrations that happen to also appear bright in the  $H\alpha$  wings (“pseudo-EBs”, Rutten et al. 2013).

Next, we define “flaring arch filaments” (henceforth FAFs) as sudden fierce brightenings in AIA 1600 Å image sequences that differ from the EB brightenings also seen in this AIA channel by appearing with shorter duration and more abrupt changes, having elongated morphology, and showing fast apparent brightness motion along filamentary strands. Because they are usually much less evident in AIA 1700 Å images, their 1600 Å appearance is likely due to brightening of the C IV doublet at 1548 and 1550 Å in AIA’s 1600 Å passband. Their filamentary morphology and rapid evolution suggest that these are heating events, likely reconnection, that take place along the fibrillar canopy seen e.g., at  $H\alpha$  line center, or eject heated matter along chromospheric field lines.

Finally, we define “IRIS bombs” (henceforth IBs) following Peter et al. (2014) as ultraviolet brightenings with substantial emission in the Si IV lines observed by IRIS, and showing these with very wide and complex non-

Gaussian profiles on which deep absorption blends of lower metal ionization stages are superimposed.

The visibility of EBs in AIA’s 1700 Å images and the wonderful full-time full-disk availability of SDO data enables one to check any new observational EB study to ascertain that it does not instead address pseudo-EBs or FAFs. We did so for the EB literature since [Paper I](#) and briefly comment on our scrutiny here.

We judge that the 3570 EBs of [Nelson et al. \(2013a\)](#) were probably pseudo-EBs, and likewise the 4 EBs of [Nelson et al. \(2013b\)](#). Both studies targeted decaying sunspots rather than emerging active regions.

In contrast, we recognized the 3 EBs of [Bello González et al. \(2013\)](#) as well-defined EBs in 1700 Å, indeed occurring in a complex region with much flux emergence. Similarly for at least EB3 and EB4 of [Hong et al. \(2014\)](#) and the single EB of [Yang et al. 2013](#) (which occurred a day after those of [Bello González et al. 2013](#) in the same region). Most recently, the near-limb EBs in [Nelson et al. \(2015\)](#) have obvious flame morphology.

Generally, the latter papers confirm our view in [Paper I](#), [Paper II](#), [Rutten et al. \(2013\)](#). EBs are strong-field opposite-polarity cancellations that occur in complex emerging active regions. They mark reconnection taking place in the photosphere, and produce substantial local heating that leaves no direct signature in the overlying chromosphere and transition region.

Modeling of the H $\alpha$ -wing enhancements that characterize EBs was recently reported by [Nelson et al. \(2013b\)](#), [Bello González et al. \(2013\)](#), [Hong et al. \(2014\)](#), and [Berlicki & Heinzel \(2014\)](#). We return to these analyses in Sect. 4, but already point out here that they agree with all earlier modeling in claiming upper-photosphere temperature enhancements of only 1000–5000 K, in obvious conflict with the notion that EBs might be IBs for which [Peter et al. \(2014\)](#) suggest formation temperatures near 100 000 K.

Were the IBs of [Peter et al. \(2014\)](#) indeed EBs as suggested by them? Our similar inspection of the concurrent AIA 1700 and 1600 Å morphology turned out indecisive. Their bomb B-1, with deep Ni II and Fe II absorption blends in the Si IV lines, seemed a bonafide EB to us but the others looked more FAF-like. Hence, as stressed by [Peter et al. \(2014\)](#), there is a clear need for simultaneous IRIS and ground-based H $\alpha$  observation of EBs and IBs because EB recognition is easier in H $\alpha$ .

In this paper we address this EB–IB issue by combining new EB and FAF observations with the SST with simultaneous observations with IRIS and SDO/AIA. Our conclusion is that both EBs and FAFs produce ultraviolet line profiles of IB type, and that these provide valuable insights and constraints.

The observations are presented in the next section, the results in Sect. 3. We discuss them in Sect. 4 and add conclusions in Sect. 5.

## 2. OBSERVATIONS, REDUCTION, METHODS

### 2.1. Data collection

For this study we analyzed data from multiple observing campaigns targeting emerging active regions with co-pointing of the SST and IRIS. The SST’s CRisp Imaging SpectroPolarimeter (CRISP; [Scharmer et al. 2008](#)), a Fabry-Pérot interferometer, collected imaging spec-

troscopy in at least H $\alpha$  (further specification in Table 1).

The IRIS spectrograph (SG) recorded its standard selection of ultraviolet lines: the C II doublet near 1335 Å, the Si IV doublet at 1394 Å and 1403 Å, the Mg II and k lines near 2796 Å and 2804 Å including the overlapping part between them with various blends, in particular the Mg II triplet lines near 2798 Å (which are two overlapping transitions that overlap so closely that they look like one line in the spectrum). For more details including characteristic formation temperatures see Table 4 of [De Pontieu et al. \(2014\)](#). For IRIS-related formation studies of Mg II and k see [Leenaarts et al. \(2013a\)](#), [Leenaarts et al. \(2013b\)](#), and [Pereira et al. \(2013\)](#); see [Pereira et al. \(2015\)](#) for a similar formation study of the Mg II triplet lines. In addition, IRIS collected slitjaw images (SJI) in the 1330 Å, 1400 Å, 2796 Å and 2832 Å channels, as detailed in Table 3 of [De Pontieu et al. \(2014\)](#).

In Table 1 we specify pointing, spectral and timing details for the three particular datasets from these co-ordinated observing campaigns that were selected for this paper.

The top row of Fig. 1 shows image samples of the first. It covered the major sunspot in active region AR 11836 that had a pronounced moat flow. IRIS supported these observations in a “4-step sparse raster” mode of slit motion, covering 3 arcsec with 2 s exposure times per step. This pattern gives good temporal resolution for a given spot on the Sun but smaller chance of hitting a scarce feature such as an EB.

Sample images for datasets 2 and 3 covering AR 12089 are similarly shown in the lower rows of Fig. 1. For both IRIS took a dense synoptic raster of 96 steps, covering 31.35 arcsec at 4 s exposure time per step. The larger pattern width gives larger spatial chance of hitting an EB, but the consequently low repeat cadence, longer than the typical EB appearance, diminishes the catch.

We also collected corresponding image sequences from SDO/AIA and SDO/HMI ([Scherrer et al. 2012](#)) using the JSOC image cutout service at Stanford University.

### 2.2. Data reduction

The SST/CRISP data were reduced using the CRISPRED pipeline ([de la Cruz Rodríguez et al. 2015](#)). It includes (1) dark and flat field correction, (2) multi-object multi-frame blind deconvolution ([van Noort et al. 2005](#)) to reduce the effects of high-order atmospheric seeing, (3) minimization of remaining small-scale deformation through cross-correlation ([Henriques 2012](#)), (4) prefilter transmission correction ([de la Cruz Rodríguez 2010](#)), (5) correction for time-dependent image rotation due to the alt-azimuth telescope configuration, and (6) removal of remaining rubber-sheet distortions by destretching ([Shine et al. 1994](#)).

The SST and IRIS data were co-aligned using far-wing images in H $\alpha$  (dataset 1) or Ca II 8542 Å (datasets 2 and 3) and the IRIS Mg II h 2832 Å slitjaws. SDO/AIA 1600 Å or 1700 Å images (depending on the dataset) were used as initial co-location reference to define common features in the fields-of-view and their offsets. The SST data were then resampled to the IRIS slitjaw pixel size of 0.167 arcsec<sup>2</sup>. Finally, sub-images (usually containing one or more pores) were then selected manually for cross-correlation at each time step.

TABLE 1  
OVERVIEW OF THE DATASETS ANALYZED IN THIS STUDY.

Set	Date	Target			Instrument	OBSID	Diagnostic details					Time [UTC]
		AR	( $X, Y$ ) [ $''$ ]	$\theta$ [ $^\circ$ ]			Name	$\lambda_0$ [ $\text{\AA}$ ]	Range <sup>a</sup> [ $\text{\AA}$ ]	$\Delta\lambda$ [m $\text{\AA}$ ]	$\Delta t$ [s]	
1	2013 Sep 6	11836	(763, 129)	50.6	CRISP	—	H $\alpha$	6563	$\pm 1.2$	100	5.5	08:15–09:01
							SG ( $4 \times 1''$ )	—	—	—	11	08:11–11:39
					IRIS	4003004168	SJI 1330	1340	55	—	12	
							SJI 1400	1390	55	—	12	
							SJI 2796	2796	4	—	12	
							SJI 2832	2830	4	—	69	
2	2014 Jun 14	12089	(221, 278)	21.5	CRISP	—	H $\alpha$	6563	$\pm 1.4$	200	11.4	07:20–08:11
							Ca II	8542	$\pm 1.2$	100		
					IRIS	3820256197	Fe I	6302	$-0.048^b$	—		
							SG ( $96 \times 0.33''$ )	—	—	—	516	07:29–10:47
							SJI 1330	1340	55	—	17	
							SJI 1400	1390	55	—	17	
							SJI 2796	2796	4	—	17	
							SJI 2832	2830	4	—	86	
3	2014 Jun 15	12089	(411, 281)	31.0	CRISP	—	H $\alpha$	6563	$\pm 1.4$	200	11.4	07:47–08:49
							Ca II	8542	$\pm 1.2$	100		
					IRIS	3820256197	Fe I	6302	$-0.048^b$	—		
							SG ( $96 \times 0.33''$ )	—	—	—	516	07:29–10:55
							SJI 1330	1340	55	—	17	
							SJI 1400	1390	55	—	17	
							SJI 2796	2796	4	—	17	
							SJI 2832	2830	4	—	86	

<sup>a</sup> This column gives the passband width in case of the slitjaw image channels.

<sup>b</sup> Full Stokes polarization measurements were obtained at this wavelength position.

The AIA and HMI image sequences were also precisely co-aligned with the full-resolution SST image sequences.

In the alignment and the data analysis we made much use of the CRisp SPectral EXplorer (CRISPEX; [Vissers & Rouppe van der Voort 2012](#)) for data browsing. The latest version (available through SolarSoft) can handle both FITS-formatted IRIS data including slitjaw images, and legacy “La Palma”-format data files from the SST.

### 2.3. EB identification using H $\alpha$

Identifying EBs is not a trivial matter. A substantial part of the EB literature did not address actual EBs but “pseudo-EBs”: magnetic concentrations (MC) in network or plage that likewise brighten in the H $\alpha$  wings as explained by [Leenaarts et al. \(2006b\)](#). Such MC brightening is more familiar as “facular bright points” in the continuum and in the molecular G-band around 4305  $\text{\AA}$  and as “line gaps” in neutral-metal lines, but it actually reaches largest contrast in the blue wing of H $\alpha$  ([Leenaarts et al. 2006a](#)). It is well understood and is not a sign of heating but of deeper-than-normal radiation escape (summary and references in [Rutten et al. 2013](#)). Hence, care must be taken to ascertain that features that appear bright in an H $\alpha$  wing are indeed EBs and not just facular brightenings—a warning already given by [Ellerman \(1917\)](#) himself. A first check is to ascertain on the daily magnetogram movies from SDO/HMI that the observed field of view is part of an active region with much flux emergence and fast streaming motions including bipolar collisions.

In [Paper I](#) and [Paper II](#) we found that EBs are best identified using H $\alpha$  wing images with slanted viewing away from disk center. We obtain such wing images by summing the three spectral samplings of both H $\alpha$  wings

around  $\Delta\lambda = \pm 1.0 \text{\AA}$ . In limbward viewing at the SST resolution MCs reach less H $\alpha$ -wing brightness contrast than near disk center, whereas EBs appear with definite flame morphology. They show up as elongated bright upright features that rapidly flicker (hence “flames”) during a few minutes while their feet are anchored in and travel along MC-rich intergranular lanes. Their tops extend intermittently up to Mm heights. This rapid-flame behavior is the best diagnostic to classify an H $\alpha$  wing brightening as EB<sup>1</sup>.

In [Paper I](#) this flame morphology was used to identify EBs manually, but in [Paper II](#) we defined automated selection criteria employing the brightness contrast, spatial extent, temporal continuity and lifetime of candidate features in SST imaging-spectroscopy sequences sampling the H $\alpha$  wings. These criteria were tuned to optimally recover example EBs that had been identified visually from their time-dependent morphology, and then applied to obtain a faster, more objective, and more complete identification of EBs in each data set.

In the present analysis we have applied these criteria to our three datasets, but with an adjustment for dataset 2 in which we lowered the thresholds to 145% brightness contrast over the field-of-view mean for the EB kernel and 130% for adjacent pixels, instead of the [Paper II](#) values of 155% and 140%. We did so because visual inspection showed that with the latter thresholds we missed a number of features of which the morphology suggested they were EBs, even though weak in relative H $\alpha$  wing excess. A reason may be that this field of view

<sup>1</sup> We emphatically invite the reader to inspect the high-resolution EB movies available with [Paper I](#) and so become familiar with this defining morphology.



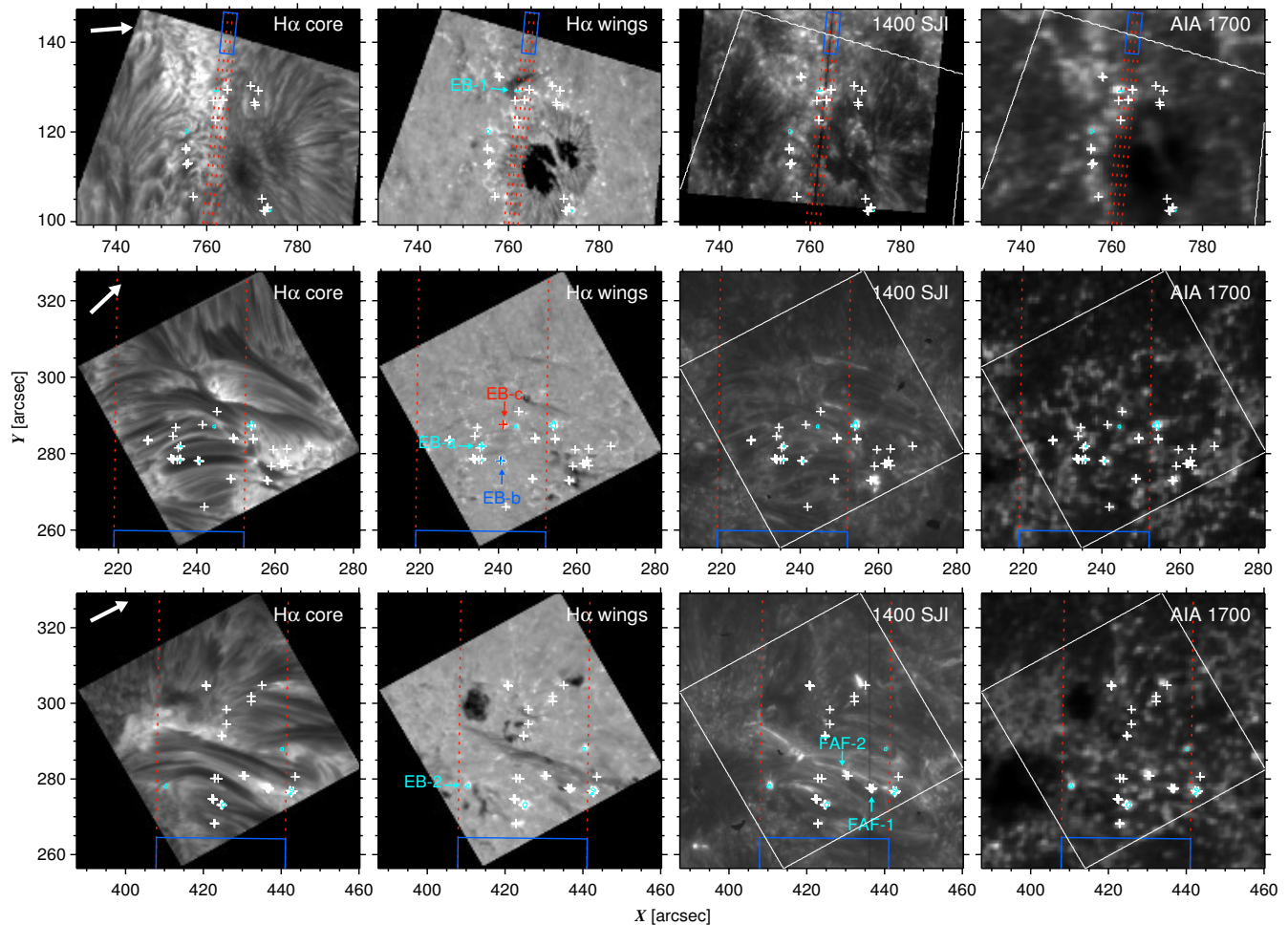


FIG. 1.— Field-of-view images from datasets 1–3 in rows from top to bottom. The SST and IRIS images have been rotated to solar ( $X, Y$ ) coordinates. *Left to right*: SST  $H\alpha$  core, SST  $H\alpha$  summed wings, IRIS 1400 Å slitjaw (SJI = slitjaw image), AIA 1700 Å. Red dashed lines specify IRIS slit locations (*top row*) or raster extent (*lower rows*).  $H\alpha$  EB detections for the instant sampled by these images are marked with cyan contours. White pluses mark  $H\alpha$  EB detections at other times in each data sequence. The selected EBs presented in detail below are identified in the second column: EB-1 in the top row, EB-2 in the bottom row, and “weak” EB-a, EB-b, and EB-c in the middle row. The position of the selected FAFs (FAF-1 and FAF-2) are indicated in the third panel of the bottom row. The white arrows in the first column specify the direction to the nearest limb. The white frames on the IRIS and AIA panels specify the SST field of view (the actual IRIS slitjaw images are larger than shown here). The blue rectangles outline the quieter areas over which IRIS spectra were averaged to obtain reference profiles. In the lower rows these extend 5.6 and 10.3 arcsec below the image cutouts, respectively. Animated versions of these panels, including SDO/HMI line-of-sight magnetograms, are available in the online edition of the journal.

contained no dark umbrae or pores and therefore had a higher mean profile than in [Paper II](#). Also, it was the closest to disk center where MCs appear brightest in the  $H\alpha$  wings.

Examples of the resulting threshold contours outlining EB candidates are shown in [Fig. 1](#) for those that were detected at the particular moment at which each image was taken. The numerous white plus signs mark other  $H\alpha$  EB detections during the whole SST observing period. Some overlap closely and are detections of repetitive EBs at about the same location.

#### 2.4. EB identification in the 1700 Å continuum

In [Paper II](#) we also tried to automate EB-finding in SDO/AIA 1700 Å image sequences. EBs typically appear in these as strongly enhanced, fairly pointlike and fairly stable brightness features. AIA 1600 Å images show them at yet larger brightness contrast above ordinary MCs, but as noted above the scene at this wave-

length often contains FAFs as well ([Rutten et al. 2013](#)).

In the less FAF-infested 1700 Å images a contrast criterion of  $8\sigma$  above the mean intensity was found to recover most of the brighter  $H\alpha$  EBs. This conservative threshold may miss weaker EBs, but lower cutoff values give more confusion with non-eruptive MCs. An additional lifetime maximum of 5 min was also set to distinguish EBs from longer-lived MCs. A further non-automated check is to ignore 1700 Å detections when they exhibit FAF behavior at 1600 Å.

#### 2.5. EB visibility in IRIS slitjaw images and spectra

Blinking of the IRIS slitjaw and the CRISP  $H\alpha$  movies suggested that bright EBs detected in the  $H\alpha$  wings often show up as bright features in the C II, Si IV, and Mg II k slitjaw images. However, the fraction for which we also have IRIS spectra is small. For dataset 1 this is obvious in the top row of [Fig. 1](#) where the narrow IRIS scan-strip missed most  $H\alpha$  EB detections (white plus signs).

For datasets 2 and 3 the IRIS raster extent was much wider so that many more  $H\alpha$  EBs fell within it, but the slow raster repeat cadence of 516 s meant that most of these were not sampled spectroscopically during their brief lifetime. Nevertheless, in the few cases of proper EB slit coverage the IRIS spectra show corresponding brightening of the major IRIS lines, so that it is probable that the slitjaw brightenings are simply set by the wavelength-integrated enhancements of these lines.

Examples are shown in Fig. 1 and yet clearer in the smaller cutout sequences in Figs. 2, 6, and 9 discussed below. In general, the bright IRIS slitjaw features are not one-to-one identical with the  $H\alpha$ -wing brightenings but there is good overall correspondence in location, orientation, shape, and evolution.

### 2.6. EB and FAF selection for presentation here

For dataset 1 application of the Paper II  $H\alpha$  criteria resulted in 31  $H\alpha$  EB detections, of which many showed pronounced slitjaw brightening. However, of those 31  $H\alpha$  EBs only 4 were sampled by the IRIS slit and only one of these showed pronounced brightening in the slitjaws. We selected the latter one for detailed presentation below and henceforth refer to this EB as EB-1. It also passed the 1700 Å criteria of Paper II, while the other three sampled by the IRIS slits did not.

Data set 2 was closest to disk center so that distinction from ordinary MCs and recognition of flame morphology was likely hampered by top-down viewing. Our down-tuned  $H\alpha$  criteria gave 49 EB detections, of which 6 were sampled spectroscopically by IRIS. Most were weak in  $H\alpha$  and the IRIS spectra, and weak or invisible in the IRIS slitjaws. We selected the three with the highest IRIS profiles and call them EB-a, EB-b, EB-c henceforth and present their spectra below as examples of weaker or even questionable EBs. Only EB-b passed the 1700 Å criteria.

For dataset 3 the Paper II  $H\alpha$  criteria yielded 56 detections of which 10 were sampled spectroscopically by IRIS. Most were weak; the exception was a very long-lived repetitive EB which we call EB-2 henceforth. It did not pass the Paper II 1700 Å criteria initially, but it did when we relaxed the constraint on lifetime to distinguish weak EBs from longer-lived MCs. EB-2 was clearly not a pseudo-EB in  $H\alpha$ . In 1700 Å it occurred repetitively for an exceptionally long period of time.

In dataset 3 we also noted a string of fierce repetitive interconnected brightenings of which the SDO/AIA 1600 Å movie shows they were FAFs. We also selected two of these for comparative display and discussion below.

A fourth SST-IRIS dataset taken on September 25, 2013 was discarded because of its 48  $H\alpha$  EB detections only one was sampled by IRIS. It did not show up in the slitjaw images and produced only slight ultraviolet line brightenings, much as the discarded EBs in dataset 2 and therefore, like those, not selected for detailed presentation here. There were more EBs visible in the latter, but outside the narrow raster strip.

## 3. RESULTS

In this section we present the observations for each selected feature in succession, using the same plot formats

for cutout samples from the SST, SDO and IRIS slitjaw images, light curves distilled from these, and IRIS spectra at selected pixels and times corresponding to the cutouts. For each feature we add some interpretation, but we postpone overall discussion to Sect. 4.

### 3.1. Details for EB-1

When viewing EB-1 in the  $H\alpha$  sequences, using CRISPEX to inspect its spatial, temporal, and spectral behavior in flexible cursor-controlled movie mode (a recommended *modus operandi*), this EB appears as a sequence of unmistakable tall EB flames in the outer  $H\alpha$  wings, re-occurring in rapid succession during the whole observing period, with fast motion of its successive foot-points away from the spot along an MC-filled lane. Our CRISPEX inspection also showed that a dark redshifted chromospheric fibril was overlying the  $H\alpha$  core part of the time.

In the AIA 1700 Å sequence EB-1 also stands out bright and EB-like, i.e., pointlike, roughly stationary, without filamentary FAF signature. The HMI magnetogram sequence shows that it occurred in a complex region with much streaming motion, from the sunspot towards extended plage and pores of both polarities further North. Small patches of opposite polarity traveled fast in this flow but were barely visible with HMI. Likely such patches produced EB-1 successively while canceling. In Paper II we observed EBs at similar cancelations of small opposite-polarity patches in SST magnetograms with better detail than given by HMI.

Unfortunately, EB-1 was sampled by the IRIS slit only at the beginning of the SST sequence and only at two positions of the narrow scan pattern. In its successive flarings EB-1 migrated eastward out of the scan strip. However, during this 10-min overlap period the rapid-scan format gave good temporal sample resolution.

Figure 2 shows a selection of small-field cutouts of EB-1 in various diagnostics. The time differences along rows are negligible by using nearest-neighbor selection, whereas the rows are about 3 min apart in order to sample EB-1's evolution. Colored plus signs specify the pixels for which IRIS spectra are shown in Fig. 4 with the same colors. The slitjaws in the last two columns of Fig. 2 show the IRIS slit as a dark near-vertical stripe at or close to the plus signs at corresponding times.

EB-1 appeared to be fairly upright, so that the red and blue pixels in the top row of Fig. 2 likely sampled its lower and upper parts (the spectra in Fig. 4 confirm this distinction). The violet pixel in the second row of Fig. 2 sampled the same location on the Sun as the red pixel in the first row, but during the 2.5 minutes between these samplings EB-1 moved to the left in its successive flaring, so that the violet pixel sampled its middle part. The morphology of the emission patches in Fig. 2 suggests that the 1700 Å feature came mostly from the lower part and that the ultraviolet images sampled increasingly more of the upper part for higher formation temperature (left to right). The  $H\alpha$ -wing brightness maps only the lower part in the top row, but in the second row EB-1 appears as an  $H\alpha$ -wing brightness patch that resembles the ultraviolet patches, whereas the 1700 Å feature remained dominated by the lower part.

The row-to-row evolution in Fig. 2 suggests that EB-1

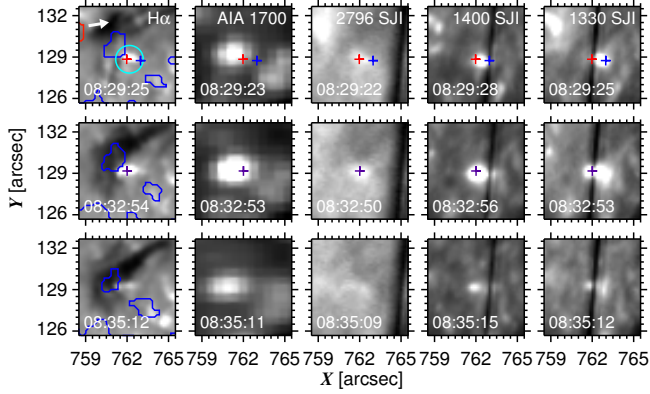


FIG. 2.— Time evolution of EB-1 in various diagnostics. *Left to right:* co-spatial image cutouts of CRISP  $H\alpha$  wings, AIA 1700 Å, IRIS Mg II k, Si IV, and C II slitjaws. Red and blue contours in the first column indicate patches of positive and negative polarity (thresholded at 0 and -1000 counts), respectively, based on the HMI line-of-sight magnetic field data. The time of observation is specified at the bottom of each panel. The plus signs mark the locations for which corresponding spectra are shown with the same color coding in Fig. 4. The cyan circle indicates the size (and instantaneous location) of the mask used to determine the light curves in Fig. 3. The arrow in the same panel specifies the “upright” direction to the nearest limb. The panels in each column have been bytescaled to the same extremes.

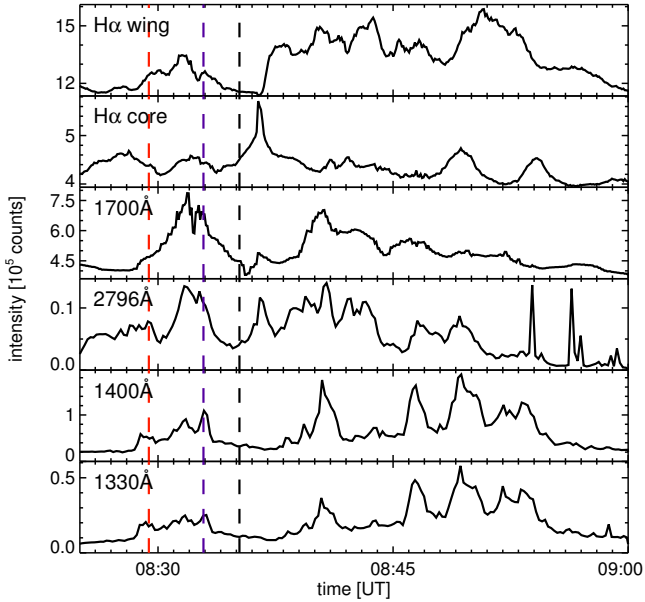


FIG. 3.— Light curves for EB-1 showing from top to bottom the intensities in the  $H\alpha$  wings and core, AIA 1700 Å, and the Mg II k, Si IV and C II slitjaws as function of time. Each intensity value is the sum over a co-moving circular aperture centered on the  $H\alpha$  detection with a diameter of 2.0 arcsec (1.5 times the maximum diameter of the  $H\alpha$  EB contour), as indicated by the circle in the first panel of Fig. 2. The presence of the slit and diffraction from it produced extra modulation of the lower three diagnostics during the first ten minutes. The vertical dashed lines mark the times per row of Fig. 2, with the same color coding. The first (red) corresponds to the near-simultaneous blue and red sampling of EB-1 in the first row, the second to the violet colored sampling in the second row, the third (black) to the EB aftermath in the third row for which we show no IRIS spectra (since not of interest).

grew from the first sample time to the second, while migrating leftward, and then diminished. This is confirmed by Fig. 3 which shows the time behavior of the integrated emission of EB-1 in the SST, IRIS, and SDO/AIA imaging. The integration area was defined appreciably wider than the  $H\alpha$  detection contour to admit the larger extent of the brightenings in the IRIS slitjaw and AIA images (Fig. 2). The first part covers the three sample times of Fig. 2 (dashed vertical lines) and shows a rise, a high peak around 08:32 UT, and a subsequent decay in all diagnostics. Subsequently there were yet more brightenings, with interesting differences between the various curves, but unfortunately without spectroscopic sampling by IRIS because EB-1 had drifted off the slit scan strip. The  $H\alpha$ -core curve shows a high peak a minute after the third sampling. Inspection showed that it was from a bright fibril ending of the type commonly seen at  $H\alpha$  line center, with many similar ones in the neighborhood. Nothing like the microflare of FAF-1 discussed below.

Figure 4 shows SST  $H\alpha$  profiles and IRIS ultraviolet-line profiles of EB-1. The color coding corresponds to the pixel markers in Fig. 2. The black profiles are the spatial average over the area specified by blue frames in Fig. 1. These reference profiles serve to gauge the amount of unusual brightening in the EB profiles.

In the first panel of Fig. 4 the red  $H\alpha$  profile from the lower part of EB-1 shows characteristic EB signature: excess wings but nothing special in the core. The blue profile from the upper part shows no  $H\alpha$  brightening yet, as already noted in the first row of Fig. 2, but the subsequent violet profile shows considerable  $H\alpha$  wing brightening. This profile also indicates significant core redshift, but this we attribute to the overlying fibril seen in the line-center movie. EB-1 contributed only the wing parts outside the steep core flanks.

If overlying fibrils are opaque in the  $H\alpha$  core, they must be much more opaque in Mg II and k for the following reasons. In Paper II we found already that the core of Ca II 8542 Å is affected by overlying fibrils similarly to  $H\alpha$ , be it with larger sensitivity to non-thermal Dopplershifts. Fibrils that appear opaque in both  $H\alpha$  and Ca II 8542 Å must necessarily be yet more opaque at the centers of the Ca II H and K lines, since these are from the Ca II ground state while the 8542 Å line is from an excited level. Such fibrils must then be 18 times (Mg/Ca abundance ratio) more opaque yet at the centers of the Mg II and k lines.

The Mg II and k cores in the bottom right panel of Fig. 4 indeed show only a small response and the 2796 Å slitjaw images in Fig. 2 show less EB brightening than the other diagnostics. However, overlying fibrils must also become transparent further out in the h and k wings, just as in the  $H\alpha$  wings. The violet h and k profiles in Fig. 4 indeed show outer-wing brightening. The 2796 Å light curve in Fig. 3 shows a peak around 08:32 UT from these broader Mg II k wings.

In contrast to the fibril-dominated  $H\alpha$  and Mg II and k cores, there is large response to EB-1 in the Si IV and C II profiles in Fig. 4 and also in the Mg II triplet lines between h and k. They all show a clear progression of excess emission for the red, blue, and violet samplings, again suggesting that the upper part of EB-1 was hot-



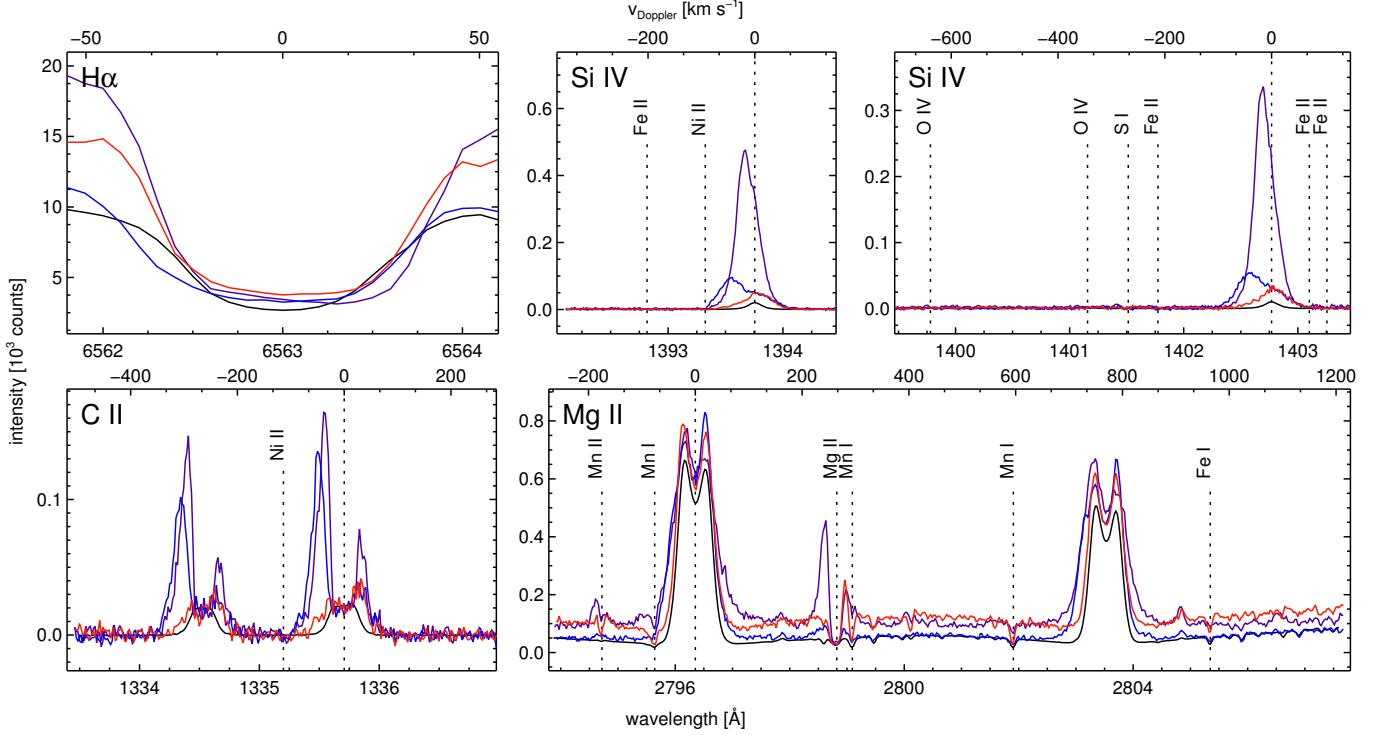


FIG. 4.— CRISP and IRIS spectra of EB-1. Clockwise:  $H\alpha$ , the Si IV lines near 1394 Å and 1403 Å, the Mg II and k lines near 2796 Å and 2804 Å with between them the (double) Mg II triplet lines near 2798 Å, and the C II doublet near 1335 Å. Several other lines and blends are indicated by labeled vertical dashed lines. All wavelengths are vacuum values (against the convention of specifying air wavelengths above 2000 Å because IRIS is a space platform). The red profiles were taken at 08:29:25 UT, the blue profiles at 08:29:28 UT, the violet profiles at 08:32:53 UT. The colors correspond to the pixel markers in Fig. 2. The black profiles show the average spectrum for the “quiet-Sun” reference box in the first row of Fig. 1. Axes: intensities in instrument units versus wavelengths in Å, with equivalent Dopplershift from line center of the strongest line along the panel tops. The second Si IV line (third panel) is drawn at doubled intensity scale to offset the factor of two between their transition probabilities; equal apparent profile heights indicate optically thin line formation.

ter than the lower part and became hotter with time. From red to blue the C II lines also became much wider. Only their central self-absorption dips remained unaffected. These are probably also fibrillar.

In addition to this brightening, the profiles of all these lines show marked asymmetries with very good correspondence between them. The redshifts of the red profiles from the lower part suggest downflow, the blueshifts of the blue and violet profiles from the upper part suggest upflow. These patterns provide direct evidence for the presence of a bi-directional flow, as discussed earlier for EBs by Shibata et al. (2007), Matsumoto et al. (2008), Archontis & Hood (2009) and in Paper I.

The blue Si IV peaks show blueshifts of roughly 30 km s<sup>-1</sup>. More precise fits with double Gaussians to reproduce their asymmetry gave blueshift magnitudes of about 45 km s<sup>-1</sup> for the main (i.e., highest intensity) components. The violet Si IV peaks for the later sampling show smaller blueshifts (about 15 km s<sup>-1</sup>) but this was the middle part of the EB, not its top, due to its Eastward progression (Fig. 2).

Thus, there is no point in inspecting (or modeling) the cores of  $H\alpha$  and Mg II and k to study EB behavior, but the striking agreement in Doppler asymmetries for the Mg II triplet, Si IV, and C II lines suggests that these sample the underlying EB without fibrillar obscuration. These IRIS lines thus provide diagnostics in which EBs are “unveiled”.

In addition, these EB-unveiling diagnostics differ

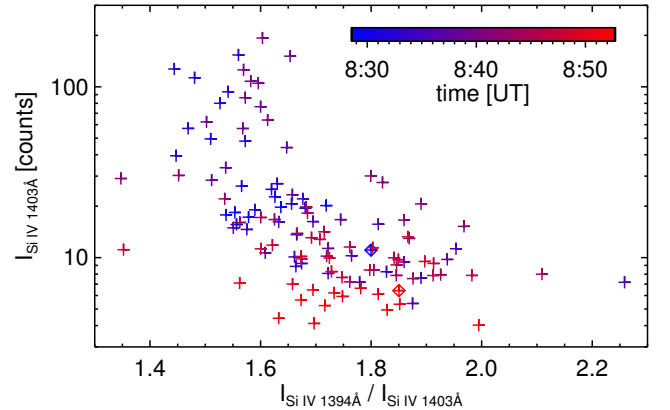


FIG. 5.— Peak intensity of the Si IV 1403 Å profile against its ratio with the peak intensity of the Si IV 1394 Å profile for all spectral samplings of EB-1. The color coding specifies observation time. The two diamonds specify the start and end samplings.

clearly in how they sample EB-1. The Si IV lines indicate a roughly optically thin feature for the red and blue profiles even at their centers, because each pair reaches similar height in the second and third panels of Fig. 4 and shows no flattening or dip in the line cores. Since the plot scales of the Si IV panels differ by the transition probability ratio, such apparent height equality suggests optically thin formation. For the violet profiles this is not the case, suggesting that the increased emissivity went together with larger EB-1 opacity.

This thickness measure is quantified in Fig. 5 which plots the intensity of one Si IV peak against the peak ratio. They were measured by averaging the profiles over all spatial-temporal samplings of pixels within the bright EB-1 patch in the 1400 Å slitjaw images that correspond to each successive IRIS scan, and smoothing the top of each averaged profile to measure its maximum intensity.

For an optically thin cloud without background irradiation the emergent doublet intensities equal the local emissivities times the geometrical thickness and obey the transition probability ratio of 2. For thicker features the ratio reduces, reaching unity for an opaque cloud with constant source function and then yielding flat-topped profiles (Fig. 2.2 of Rutten 2003). Figure 5 suggests that EB-1 was mostly neither thin nor thick, but “thinnish” with ratio values between 1.9 and 1.5 that typically correspond to thicknesses 0.3 and 1.6, respectively. The sample-time coding (color) suggests that EB-1 started and ended optically thin, but was generally somewhat thicker at high peak intensities in between.

When such features become much thicker than the photon mean free path, internal resonance scattering tends to cause outward source function decline and a corresponding central profile dip that is commonly called self-absorption. Such dips are seen in the C II lines and also in the Mg II triplet lines. However, their peak heights and asymmetries correspond very well to the Si IV profiles. Their peaks rise in concert and the higher peak of each profile is on the side to which the Si IV peaks are shifted. This good correspondence suggests that also these peaks sampled EB-1 without obscuration from overlying fibrils. The latter caused only the central dips because these show no Dopplershifts. Since the outer wings still show about similar intensities as function of wavelength separation from the line centers, the peaks and wings seem to sample the EB in optically thick fashion (otherwise they would also differ a factor of two, the transition probability ratio). For an optically thick feature the profiles represent Eddington-Barbier mapping of the source function at monochromatic optical depth  $\tau_\lambda = 1$ . In this case the different Dopplershifts of the upper and lower parts of EB-1 affect the optical depth scaling and produce the peak asymmetries. Thus, these unveiled IRIS diagnostics provide both thin and thick EB sampling.

The final features of interest in Fig. 4 are the line blends. The Si IV and C II lines are too narrow to reach the nearby Fe II and Ni II lines (rest wavelengths indicated by dashed vertical lines), but the blue wing of Mg II k and the raised overlapping wings between h and k contain strong Mn I absorption blends at 2795.64, 2799.09, and 2801.91 Å in the red lower-part sampling (best seen per zoom-in with a pdf viewer). They are weak or absent in the other samplings. We attribute them to foreground upper-photosphere gas crossed by the slanted line of sight towards EB-1 that is not part of the phenomenon and indeed imparts no obvious Dopplershift. A line of sight to the lower part then passes through the Mn I formation layer, a line of sight towards the upper part catches less or none.

The Mn II blend at 2794.72 Å shows up with interesting profiles: as a self-reversed line in the red lower-part sampling, absent in the blue upper-part sampling, but appearing with a blue-peaked profile similar to the Mg II

triplet lines at 2798.82 Å in the later violet upper-part sampling. This similarity indicates sampling of the EB itself.

In summary, the IRIS diagnostics provide an informative, understandable, and self-consistent view of EB-1 that fits very well with our earlier EB descriptions. EB-1 appeared as a photospheric below-the-fibrillar-canopy heating event with upward progression with time, larger heating higher up, and unmistakable bi-directional jet signature.

Are these EB spectra similar to the IB spectra of Peter et al. (2014)? While the C II and Si IV lines do show brightening, also with bi-directional Dopplershift signatures, their wings are not extravagantly wide. This may be a matter of timing. It is a pity that IRIS did not sample its aftermath, as is demonstrated by the next example.

### 3.2. Details for EB-2

EB-2 was sampled in IRIS spectroscopy during a longer period, but only intermittently due to the slow raster repeat at 8.6-minute cadence. Figures 6–8 display results for EB-2 in the same format as Figs. 2–4. This EB had the advantage that it appeared aligned along the IRIS slit, so that its top and bottom were spectroscopically sampled at the same time in each row of Fig. 6. The alignment was fortuitous since EB-2 was tilted considerably away from the local vertical in its azimuthal orientation (angle with the arrow in the first panel of Fig. 6).

Inspection of the SST H $\alpha$  sequences showed an unmistakable large, repetitive EB flame. EB-2 was already present at the start of the SST observations at 07:47 UT, quickly brightened, and remained nearly continuously present in the AIA image and IRIS slitjaw sequences until 08:29 UT. These image sequences and the corresponding light curves in Fig. 7 suggest that there was also preceding EB activity during fifteen minutes before the SST start. A longer-duration AIA 1700 Å sequence suggests strong repetitive EB activity at the same location already from 06:36 UT onward. The HMI magnetogram sequence shows very fast streaming with an extended patch of white polarity running into a fairly large patch of black polarity that vanished gradually and was gone by 08:30 UT. The SST magnetograms have higher spatial resolution but only at the best-seeing moments; the homogeneity of the HMI sequence makes it more suited to follow such pattern changes.

The hotter AIA diagnostics (304, 171, 193 Å) show nothing special happening at the site of EB-2 during the whole period. EB-2 thus seems a bonafide EB, but repeating over unusual duration thanks to continued supply of opposite-polarity fields.

The top row of Fig. 6 with red and blue pixel markers shows EB-2 at the start of the SST observations (first vertical line in Fig. 7). The corresponding red and blue Si IV and C II profiles in Fig. 8 appear similar in shape to those in Fig. 4, but note the differences in intensity scales: the blue and red Si IV profiles reach nearly 20 times higher count values than for EB-1, more than expected from the doubled exposure time. They are also much wider. The red C II profiles are still well separated, but the blue profiles nearly overlap. This is not seen in quiet-Sun spectra (Lites et al. 1978).



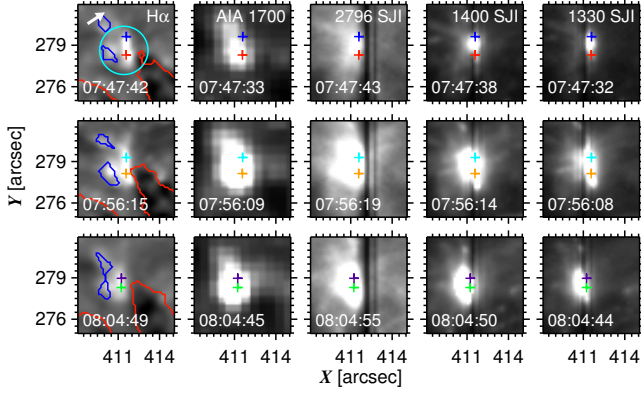


FIG. 6.— Time evolution of EB-2 in the format of Fig. 2, except that the red and blue contours in the first column are based on CRISP Fe I 6302 Å Stokes  $V$  data (thresholded at  $\pm 450$  counts). In each panel the pair of pixel markers specifies the sample locations of simultaneously recorded spectra shown in Fig. 8. The temporal separation between rows is about 8 min, larger than in Fig. 2. It corresponds to successive IRIS rasters.

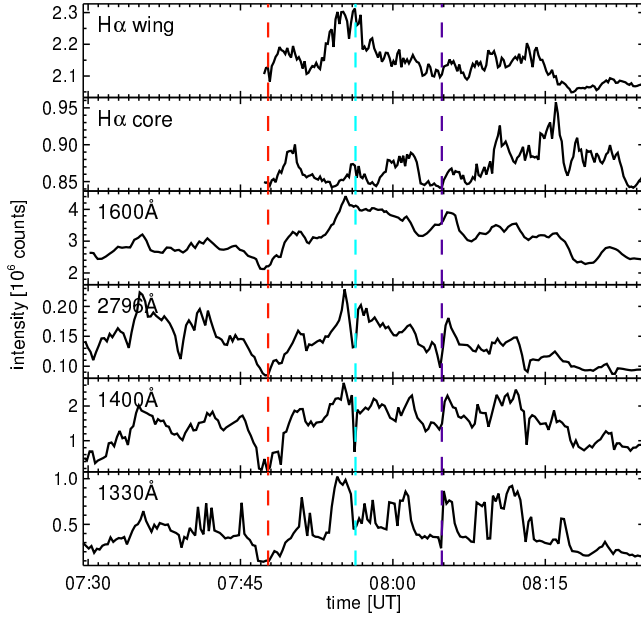


FIG. 7.— Light curves for EB-2 in the format of Fig. 3. In this case the integration aperture had a diameter of 3.5 arcsec (1.5 times the maximum diameter of the H $\alpha$  detection contour), as indicated in the first panel of Fig. 6. The three dashed vertical lines correspond to the sampling times of the three rows in Fig. 6. There are corresponding dips in the lower three curves from the slit presence over the feature.

The red and blue profiles nevertheless still display similar profiles as EB-1: clean humps with the blue ones from the upper part reaching higher intensities than the red ones from the lower part, and with redshifts for the lower sampling and blueshifts for the upper sampling that again correspond very well between the Si IV, C II, and Mg II triplet lines. As in EB-1, the 1700 Å brightness patch in the top row of Fig. 6 favors the bottom part of EB-2 while the ultraviolet images indicate higher formation for hotter diagnostics. These EB-2 results are in excellent agreement with our EB-1 findings.

However, the red and blue profiles sampled only the start-up of EB-2. It became much larger and brighter

afterwards (cf. Figs. 6 and 7). Figure 8 adds lower-and-upper spectral sample pairs also at the times when the IRIS slit passed EB-2 again around 07:56 UT and 08:05 UT, respectively (second and third rows of Fig. 6, with orange and cyan lower/upper markers in the second row and green and violet lower/upper markers in the third row). The Si IV and C II lines grew considerably in intensity and developed more complex profiles that do show IB signatures: wide wings, cores with complex structure, and deep blends.

The orange and green lower-part samplings show the most complex double-peaked Si IV profiles in Fig. 8. These profiles come closest in shape to the double-peaked profiles in Peter et al. (2014), which were interpreted as signature of a bi-directional jet. Here, the small Si IV line-center dips may represent self-absorption in stationary gas, but also just lack of stationary gas in optically-thin emissivity mapping of two counter streams as blue- and redshifted profile humps. In contrast to the similarity of the two Si IV profiles in Peter et al. (2014), the green and orange Si IV profiles of EB-2 differ between the two lines.

The Dopplershift patterns are again consistent between the different unveiled diagnostics. All lower-part samples (red, orange, green) show redshifts domination, the upper-part samples (blue, cyan, violet) single blueshifted peaks, although with redward profile tails. Most profiles show ragged tops. Such core raggedness is further discussed in Sect. 4.

The Ni II blends at 1393.32 Å in the stronger Si IV line and at 1335.20 Å between the C II lines are very pronounced in all but the red samplings. The Fe II blends at 1403.10 Å and 1403.26 Å in the red wing of the weaker Si IV line are present in the orange and green lower-part samplings, and weakly in the final violet upper-part sampling. These blends generally show blueshifts, larger in the orange than in the subsequent green sampling. They suggest upward, decelerating motion of cool gas along the line of sight to the EB.

The three lower-part samples (red, orange, green) show the Mn I blends in the Mg II and k wings, strongest in the red start-up lower sampling, whereas they are not present in the three upper samplings. We again attribute these blends to undisturbed upper-photosphere gas along slanted lines of sight to the EB foot, with lines of sight towards the upper part passing over the Mn I formation layer. In this case the Mn II line is only weakly present in the lower-part samplings, without EB sampling.

The core of H $\alpha$  remained similar in the various samplings, again indicating domination by overlying fibrils. The same holds for the line-center dips of Mg II and k. The green H $\alpha$  and h and k cores show similar redshift.

The Mg II and k peaks brightened considerably in the cyan upper-part sampling (the dip in the 2796 Å light curve in Fig. 7 is due to the slit). This curve tracks the 1700 Å light curve fairly well. Since also the peak asymmetries correspond with those of the C II lines the fibrillar obscuration may have been thinner for this sampling. The cyan H $\alpha$  core is also relatively narrow.

The outer wings of the Mg II and k seem to sample EB-2 in optically-thick manner because they have about equal intensities in the two lines (which also have a transition probability ratio of two).

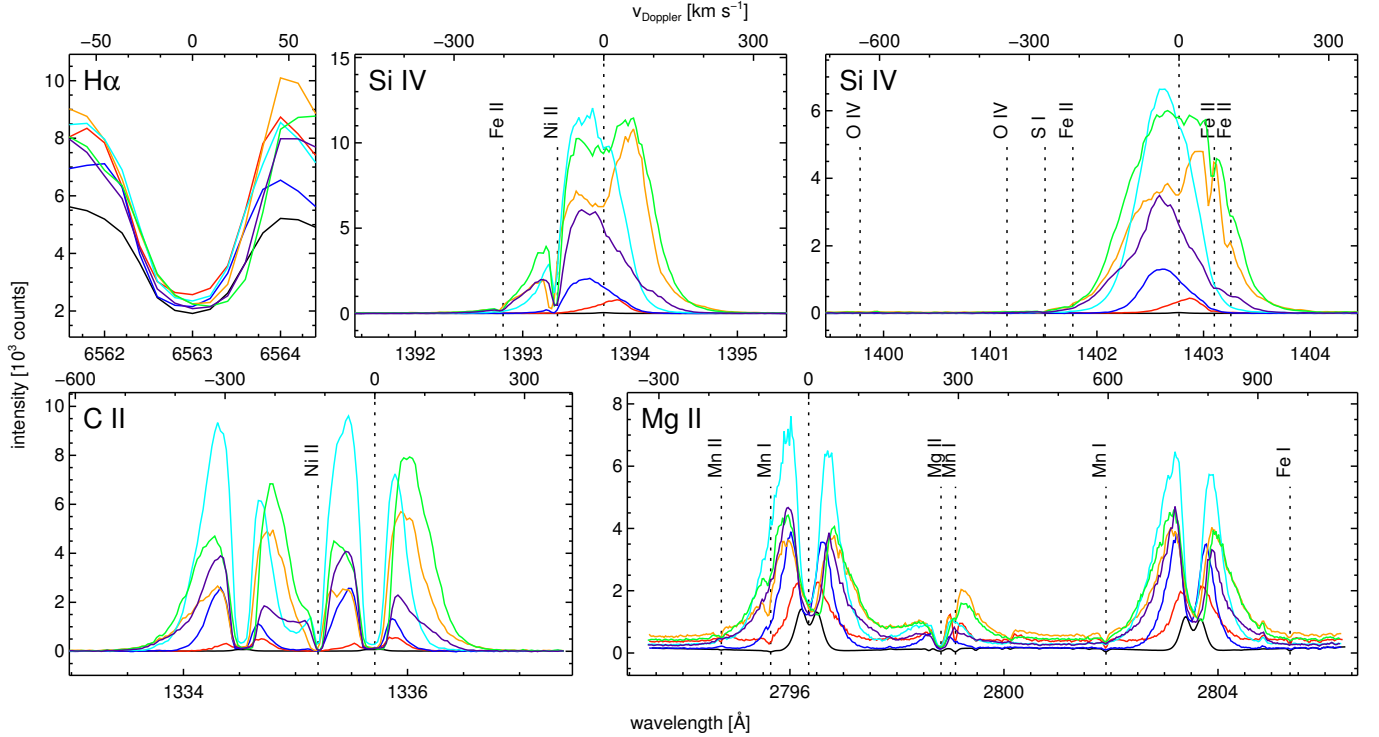


FIG. 8.— CRISP and IRIS spectra of EB-2 at the marker positions in Fig. 6, with the same color coding. The red and blue profiles were taken at 07:47:38 UT, the orange and cyan profiles at 07:56:14 UT, the green and violet profiles at 08:04:45 UT. Format as for Fig. 4, except that the H $\alpha$  panel is compressed in wavelength to make place for wider Si IV 1394 Å profiles conserving their Doppler velocity scale.

We conclude that EB-2 showed EB-1-like profiles in its onset and later developed more outspoken IB signatures. Whether EB-1 did the same we do not know, but EB-2 shows that strong EB activity can indeed produce IB-type spectra as suggested by [Peter et al. \(2014\)](#).

The similarity of the orange and green lower-part profiles and the similarity of the cyan and violet upper-part profiles at 8.6 min sampling delay suggests that the feature persisted over long duration.

Such a hot signature was not seen at the onset of EB-2, implying that the preceding hour of EB activity suggested by the AIA 1700 Å movie had not left one by that time.

### 3.3. Details for EB-a, EB-b, EB-c

EB-1 and EB-2 were well-defined strong EBs. We now turn to the weaker or questionable EB-a, EB-b, EB-c in dataset 2. Figures 9 and 10 show their sampling and spectral profiles in the format of Figs. 2 and 4.

The HMI magnetogram sequence displays a complex region with much streaming motion in which opposite-polarity patches canceled frequently. There were strong H $\alpha$  EBs that appeared as obvious 1700 Å ones, but these were unfortunately not sampled by IRIS. As noted above, we lowered the H $\alpha$  discrimination level to include weaker events that were sampled by IRIS because their H $\alpha$  morphology indicated EB nature rather than MC nature, although such recognition was hampered by more vertical viewing than in datasets 1 and 3. In the AIA 1700 Å movie none of these appeared as an obvious EB (even though EB-b passed the [Paper II](#) 1700 Å criteria). For example, in the first two panels of Fig. 9 the H $\alpha$  feature appears EB-like, but the neighboring normal MCs

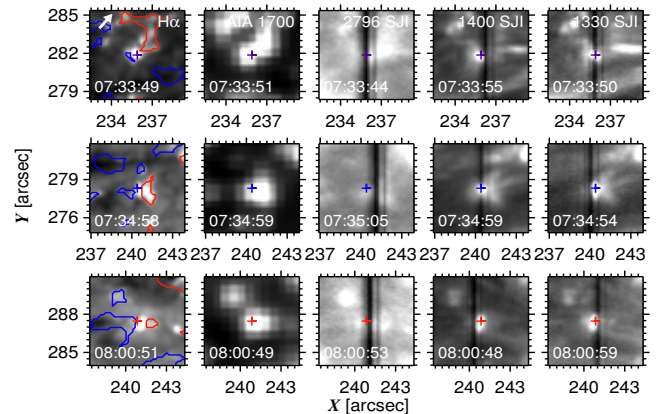


FIG. 9.— Image cutouts for EB-a (*top row*), EB-b (*middle row*) and EB-c (*bottom row*). The format is the same as for Fig. 6, except that the rows are for different locations and all panels were therefore bytescaled individually. The red and blue polarity contours represent thresholds of +100 and -250 counts, respectively.

appear as bright in 1700 Å.

The three EBs we selected for display are the ones with the highest intensities in the Si IV lines. They are sufficiently high to confirm that these candidates were not pseudo-EBs (ordinary MCs; if they were, IRIS would show such profiles from network everywhere). We therefore present these as non-suspect but weak EBs.

In Fig. 10 the Si IV lines reach about twice as high values as EB-1 in Fig. 4 which could be explained from the doubling of the exposure time), but these Si IV profiles are more complex. The apparent Si IV height equality between the differently scaled panels again indicates thinnish formation, with the non-Gaussian shapes suggesting viewing through multiple Dopplershifted compo-

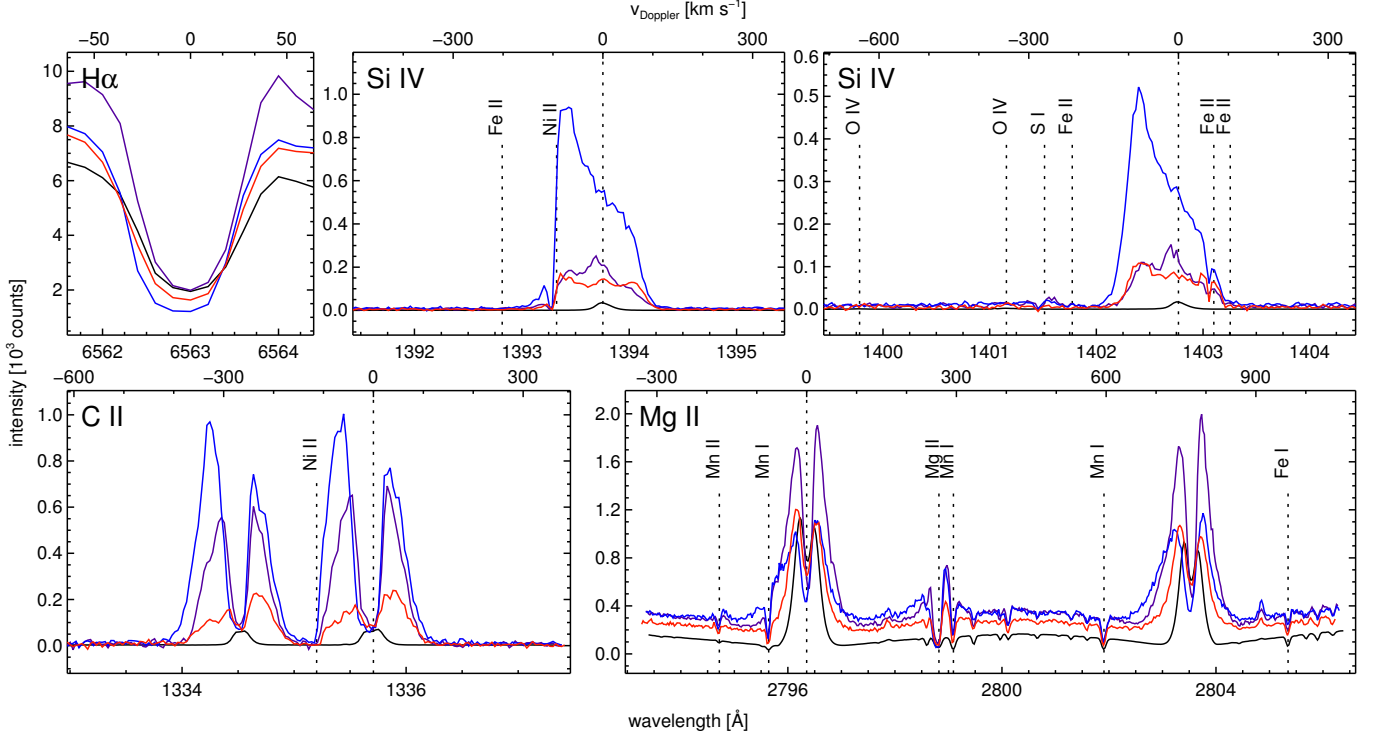


FIG. 10.— CRISP and IRIS spectra of EB-a (violet), EB-b (blue), and EB-c (red) in dataset 2 at the marker positions in Fig. 9 and with the same color coding. Format as for Fig. 4.

nents. This strengthens our judgment from Paper I and Paper II that slanted EB viewing helps to diagnose EB formation. In Figs. 4 and Fig. 8 it did by spatially separating the different Dopplershift signatures of the lower and upper parts of the bi-directional jet. Here, these likely mixed together along the line of sight in all three EBs.

Thus, the Si IV profiles in Fig. 10 suggest that the line of sight sampled both a blueshifted upper part and a redshifted lower part, with the upper part again hotter for EB-b (blue profiles) but with about equal contributions for the other two. All Si IV cores show small-scale raggedness (Sect. 4).

The C II profiles are similar to those of EB-1 in Fig. 4 but with closer peak equalities that again suggest bi-modal sampling. For EB-b the blue profile of the Mg II triplet lines shows opposite asymmetry to the blue Si IV and C II profiles, suggesting peak formation in the lower part similar to the three lower-part samples of EB-2 in this line in Fig. 8.

The various blends are markedly present in all three samplings. The Fe II and Ni II blends again show substantial blueshifts, the Mn I and Mn II lines in the last panel none. In top-down viewing as suggested by the jet mixing, the latter must be from cool upper-photosphere-like gas above the EBs, suggesting that the EB flames did not reach high into the atmosphere.

The upshot is that these three weak EBs adhere to the pattern set by EB-1 and EB-2 in their start-up phases, but without spatially resolving the bi-directional jets. It is better to observe EBs away from disk center, which also increases EB contrasts over MCs at 1700 Å.

### 3.4. Details for FAF-1

In dataset 3 a string of very bright FAFs appeared in the lower part of the field of view in Fig. 1, East of EB-2. We selected two for display in Figs. 11–16. Their locations are specified in Fig. 1.

Blinking the AIA 1700 Å and HMI magnetogram movies shows that FAF-1 started when a small patch of black polarity ran fast from afar to merge with a larger black one adjacent to yet a larger patch of white polarity; all black polarity then vanished. FAF-2 occurred next to a fairly large black-polarity patch that moved steadily East into a weak diffuse, barely visible, white-polarity patch.

FAF-1 exhibited the strongest and most FAF-like flaring, at 08:05 UT. It did so not only in AIA 1600 Å but also in the H $\alpha$  core, appearing as a very bright microflare. At about that moment, filamentary arch-shaped brightenings extended from it and connected to two others, FAF-2 to the North-East and another FAF to the South-West. Both then brightened in tandem. EB-2 also flared again at 08:05 UT (Fig. 7), but inspection of the AIA 1600 Å movie does not suggest a filamentary connection from FAF-1.

The double filamentary arches extended at apparent speeds over the surface of 200 km s<sup>-1</sup> and then around 08:10 UT gave the impression of lifting off upward in the form of a bright thin arc-shaped thread, or giving such an appearance from successive brightening of a fan of adjacent higher-up field loops, over a length of about 20 arcsec and with an apparent projected rise speed of about 40 km s<sup>-1</sup>. This apparent lift-off was vague in AIA 1600 Å but produced a very bright arch besides FAF-1 in AIA 304, 171, and 193 Å during four minutes, with the same morphology in these diagnostics. Thus, in contrast to EBs which do not excite response in the hotter AIA



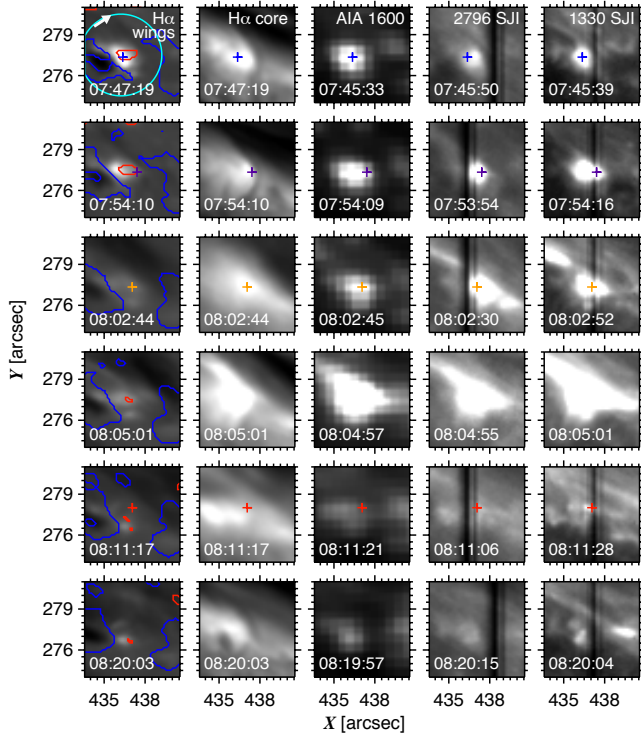


FIG. 11.— Image cutouts for FAF-1. Format as for Fig. 6, except that SST H $\alpha$  core images are added in the second column, AIA 1600 Å images instead of 1700 Å images are shown in the third column, and no 1400 Å slitjaw images are shown because they were all nearly identical to the 1330 Å ones. The red and blue polarity contours represent thresholds of +100 and -450 counts, respectively. The sample times correspond to five successive (8.6 min apart) slit samplings of this location in the IRIS raster pattern, plus the moment of the H $\alpha$  microflare (4th row). The bytescaling is the same along columns.

channels, FAF-1 did so very markedly.

Inspection of the IRIS spectra showed no spectacular profiles from this million-Kelvin arch: the Si IV lines were enhanced but single-peaked, the C II lines enhanced and double-peaked but fairly average in width, Mg II and k were enhanced and broadened, and there was no sign of the Mg II triplet lines. However, the O IV lines at 1399 and 1401 Å were clearly present throughout the hot arch. These signatures merit further investigation, but studying and displaying such hot coronal FAF aftermaths falls outside the scope of this EB paper. We concentrate here on the lower-atmosphere signatures at the FAF-1 site.

Unfortunately, the IRIS slit did not sample FAF-1 at the time of its H $\alpha$  flaring and filamentary extension. We therefore display the imaging at this time in the fourth row of Fig. 11 and show spectra from all slit passes before and after. In the fourth row the H $\alpha$  core shows its microflare while the onset of the filamentary extensions is clearest in the 1330 Å slitjaw image, but also noticeable in H $\alpha$ . There was no enhancement of the H $\alpha$  wings, nothing like an EB, at that time.

However, the first row of Fig. 11 displays brightness patches like an EB, but with the abnormality of also appearing in the H $\alpha$  core. The latter is not very bright at this initial sampling time in Fig. 12, but this is due to the presence of an extended dark fibril within the wide integration contour. The corresponding blue profiles in

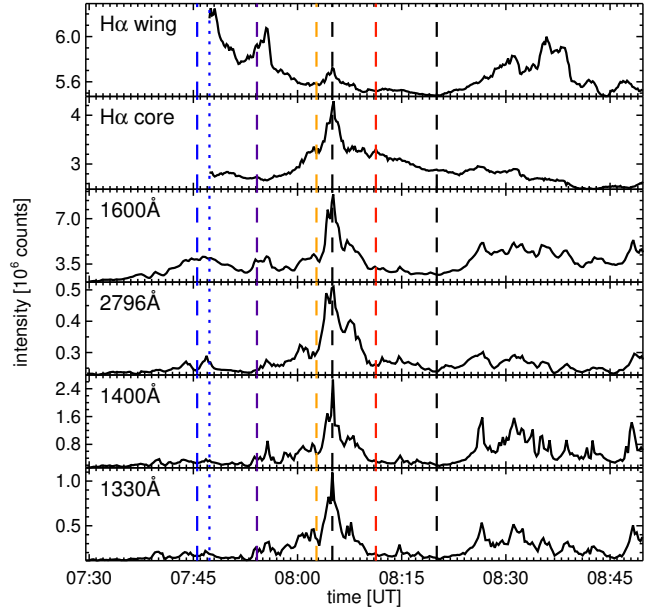


FIG. 12.— Light curves for FAF-1 in the format of Fig. 3. The integration aperture had a diameter of 6.0 arcsec, as indicated in the first panel of Fig. 11. The vertical lines correspond to the sampling times of the rows in Fig. 11. The dotted one is for the first H $\alpha$  sampling, slightly offset from the first IRIS sampling because the SST observation started at 07:47 UT.

Fig. 13 appear EB-like, rather like EB-1's violet profiles in Fig. 4 but higher, also in Mg II and k. The blue Mg II triplet profile shows very high peaks, also as for the violet sampling of EB-1.

The next sampling (second row, violet pixel and violet profiles) produced bright Si IV and C II lines. They remain less intense than the brightest from EB-2, but show extremely wide and much blueshifted profiles, top raggedness, and deep Ni II blends. The deep self-absorption dips of the C II lines remain at their rest wavelengths but the rest of the profiles are so much blueshifted, as are the Si IV lines, that almost no red peaks remain. The intensity ratio of the Si IV lines still suggests thin to thinnish formation. Both Si IV lines resemble the Si IV profiles for B-2, 3 and 4 in Peter et al. (2014), while the C II lines are most alike the C II lines for B-3 and 4, suggesting that those three IBs may in fact have been FAFs.

The striking shape similarities between the C II and Si IV profiles blueward from the nominal line centers and in the red tails suggest similar sampling of FAF-1 in these parts of the C II lines, i.e., that the profile structure is mostly set by similar effects of Dopplershift, respectively on the emissivity in optically-thin formation and on the optical depth scales in optically-thick formation.

The non-shifted C II core dips suggest formation (likely scattering) in a non-disturbed overlying region. The violet Mg II and k profiles also show wide wing extensions, with the near equality of the two lines again suggesting optically thick formation. The violet Mg II triplet profile is about normal (nearly absent). The Mn I blends in the blue h and k wings are deep dips.

The next sampling, again 8.6 min later but still 3 min before the H $\alpha$  microflare, produced the extraordinary orange profiles in Fig. 13. The Si IV and C II lines have

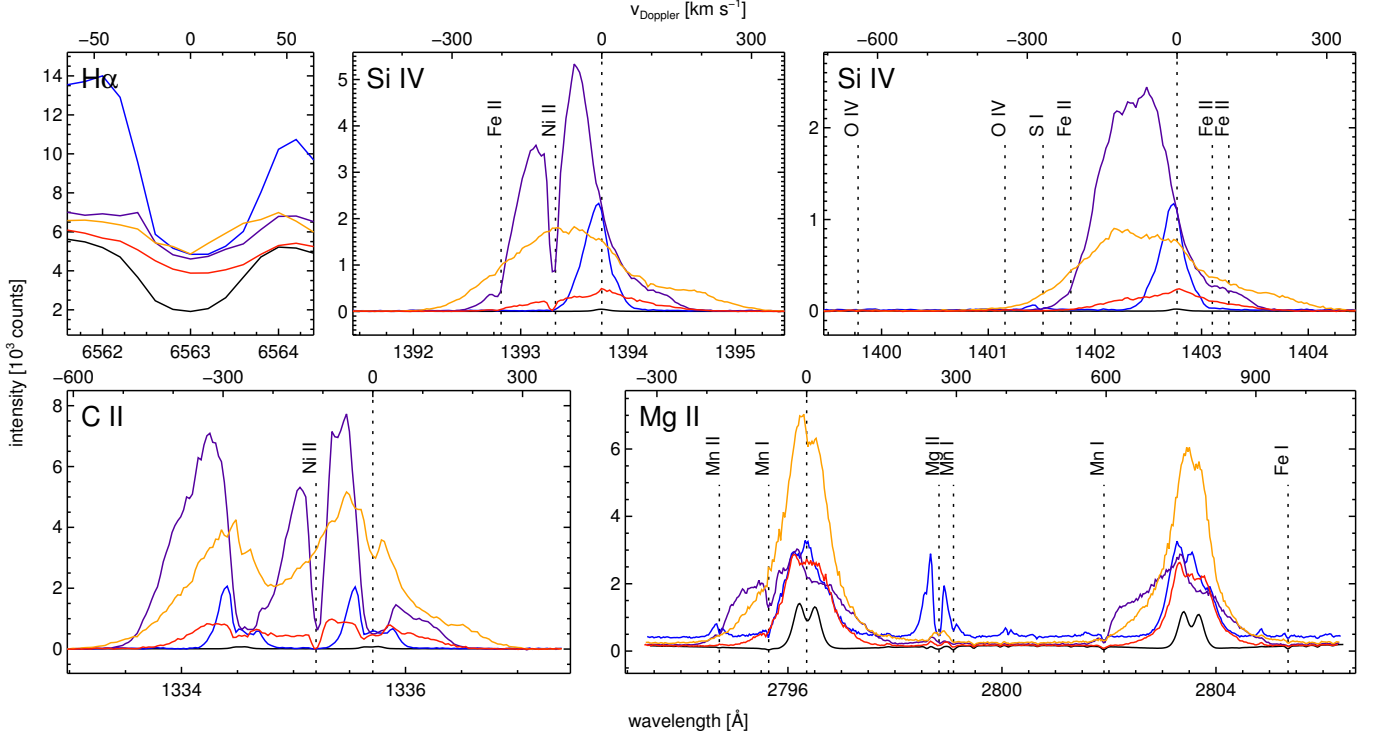


FIG. 13.— CRISP and IRIS spectra of FAF-1 at the pixels marked in Fig. 11. Format as for Fig. 4.

lower intensities, but are much wider and more symmetrical, as if smeared by enormous thermal broadening or sampling a wide distribution of very fast motions. They are appreciably blueshifted, but have extended red tails. The C II lines again appear very similar to the Si IV lines, except for the little dips at their nominal line centers suggesting minimal absorption (scattering) in undisturbed gas along the line sight. There are no absorption blends whatsoever. The profile tops are ragged.

The orange Mg II and k profiles reach as high intensities as the brightest from EB-2 and with similar profiles but show only very small central dips, with ragged appearance. They are the only h and k sampling in all our spectra with obviously unequal wing intensities between the two lines. The cores share in this behavior. The ratio is about 1.5. The orange C II profiles show similar difference. It suggests that these lines sampled FAF-1 less thickly than our other EB and FAF measurements.

The Mg II triplet lines show slight emission. Together, the orange profiles suggest sampling a very hot rising event with much internal motion that was similarly sampled by the Si IV, C II, and h and k lines, with only a small amount of undisturbed gas causing dips at the C II and h and k line centers. It indeed seems an event on its way to become a bright million-Kelvin feature in the AIA diagnostics, becoming thin or thinnish even in Mg II and k.

The next IRIS sampling came 6 min after the H $\alpha$  microflare (fifth row, red pixel, red profiles) and while the bright million-Kelvin AIA arch was present to the North-East (directly above FAF-1 it was at a height of about 6000 km and appeared projected well beyond the line of sight to FAF-1). These profiles are rather like the orange ones, but have lower intensity and are less blueshifted. They still have red tails but longer blue ones, show small

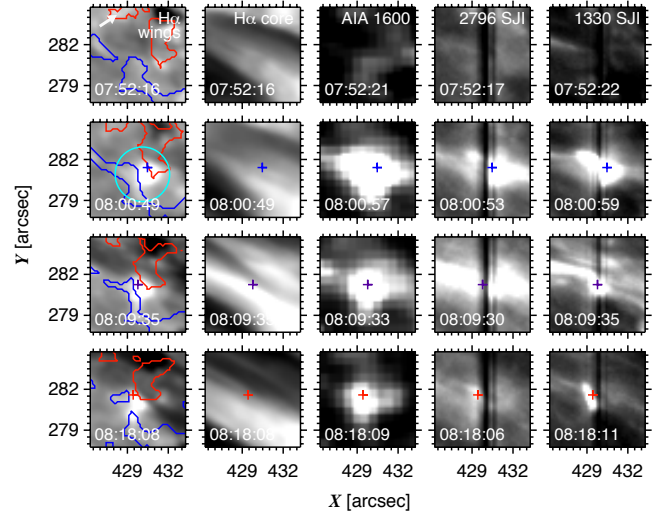


FIG. 14.— Image cutouts for FAF-2 in the format of Fig. 11, with opposite polarity contours at thresholds of  $\pm 500$  counts.

C II line-center dips, have deep Ni II blends but no Fe II blends, only very weak Mn I blends, and ratios departing from optical thickness. There was no specific brightening in the image cutouts anymore, except the H $\alpha$  core which shows a long post-flare tail in Fig. 12. In summary, the red profiles suggest a cool-down aftermath.

In the last row of Fig. 11 we also show the scene in the next IRIS sampling, in order to illustrate that the show was over. There was nothing of interest in the spectra (not shown) anymore.

### 3.5. Details for FAF-2

FAF-2 occurred close to FAF-1 but brightened earlier. It also showed double filamentary extensions in

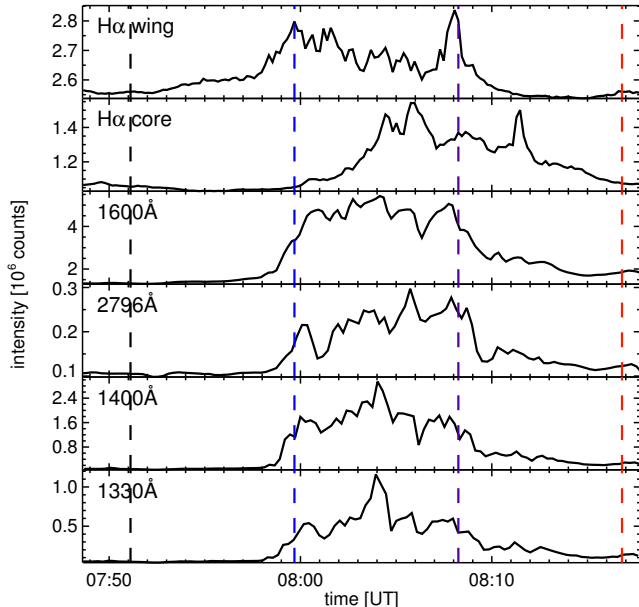


FIG. 15.— Light curves for FAF-2 in the format of Fig. 12. The integration aperture had a diameter of 4.0 arcsec, as indicated in the second panel of Fig. 14.

1600 Å and also seemed to excite response in the hotter AIA channels: slender bright arches during 08:01:30–08:03:30 UT that were clearest in 171 and 193 Å and showed up as bright narrow arcs hovering over FAF-1 in projection to the North-East, but much less prominent than the bright arch after FAF-1.

Figures 14–16 display our standard-format results for FAF-2 in four successive IRIS samplings. The first sampling (top row of Fig. 14, first vertical time marker in Fig. 15, no spectra since not of interest) shows the scene seven minutes before FAF-2 brightened: nothing special. The second and third samplings bracket its largest brightness; in the fourth it had diminished (Fig. 15). The H $\alpha$  core showed fibrillar brightening parallel to the filamentary extensions at 1600 Å but not co-spatially.

The blue profiles in Fig. 16 are the widest of all our specimens and have deep absorption blends (also from Si I and Mn II). They even show central dips in the Si IV lines. In this event the Mg II and k lines share fully in the Si IV and C II behavior. The similarity between the blue profiles of these six lines is striking, except that the peak ratios reverse from blue-over-red for Mg II and k and the C II lines to red-over-blue for the Si IV lines.

The central dips of the Si IV lines are not due to optically thick self-absorption because they do not have the same absolute intensity but still share the probability-corrected value. They suggest absorption (scattering) in stationary, likely undisturbed, gas along the line of sight that reaches sufficient opacity for thick self-absorption scattering in the C II and Mg II and k lines. Outside these cores the six lines exhibit strikingly similar profile shapes.

The blue profiles are not only the brightest but also display the largest raggedness. Inspection of the original spectral images suggests that most of the deeper narrow dips are unidentified blends (for example the dips just red and blue of the Ni II line between the C II lines). The Mn I and Mn II lines in the h and k wings are also strongly present, in this case with significant blueshifts.

The later samplings (violet and red) show roughly similar profiles at diminishing intensities. The violet sampling shows peak redshift for the Si IV lines and corresponding red-over-blue peak asymmetry for the C II lines, but not for Mg II and k. The yet later red sampling shows small peak blueshift in the Si IV lines, but similar slight blue-over-red C II and Mg II and k peak asymmetries and similar line-center redshifts in these doublets (also in the H $\alpha$  core). The blend blueshifts (also of the Mn I lines) became smaller than in the blue sampling. The Mg II triplet lines show up in absorption in all three samplings. All profiles show some core raggedness.

In summary, FAF-2 showed yet wider profiles than FAF-1 but with more symmetry and with also the Mg II and k wings taking part. The later samplings again suggest a cool-down phase, but with more undisturbed gas along the line of sight because there was no blend-free sampling as the orange profiles of FAF-1 in Fig. 13; in contrast, blends including the Mn I lines were present in all three samplings, strongly so in the first (blue) and last (red) ones. We speculate that our slanted viewing passed through undisturbed gas at larger height than the FAF samplings because fibrillar canopies tend to rise steeply away from network (containing the reconnecting MCs) to quieter internetwork areas.

## 4. DISCUSSION

### 4.1. EB and FAF properties

EBs and FAFs show interesting similarities and differences. Both phenomena occur in emerging active regions and both probably mark reconnection. EBs do this for reconnection of strong near-vertical fluxtubes in the photosphere and appear as upright flames that remain under the fibrillar chromospheric canopy (cf. Paper I, Paper II, further references in Rutten et al. 2013), or even below the upper photosphere when weak (EB-a, b, c). FAFs show distinctive fibrillar morphology and are likely reconnection events along the curved fields that define the canopy.

FAF-1 may have started below the canopy (but was then bright in the H $\alpha$  core, therefore formally not an EB) but broke through and even became an H $\alpha$ -core microflare at 08:05 UT, two minutes after it showed its widest ultraviolet profiles (orange in Fig. 13).

FAF-2 seemed to reach less high since the blends and line-center dips in all samplings in Fig. 16 suggest undisturbed cooler stationary gas along the line of sight.

Both EBs and FAFs show outspoken bi-directional jet signatures. For the EBs this is obvious since the IRIS spectra of EB-1, the onset of EB-2, and of EB-a, b, and c all show them directly, spatially separated for the first two but mixed up along the line of sight for the other three. The bi-directional nature of the FAFs is more complex because they are less aligned with the line of sight (since also seen in the images as rapid filamentary extensions) and cover larger temperature ranges. The striking difference between the violet sampling of FAF-1 and the blue sampling of FAF-2 in the IRIS profiles may simply be that the first sampled only one of such jets, the other both. The IRIS profiles from B-1 of Peter et al. (2014) then fit in this picture by showing larger Doppler separation.



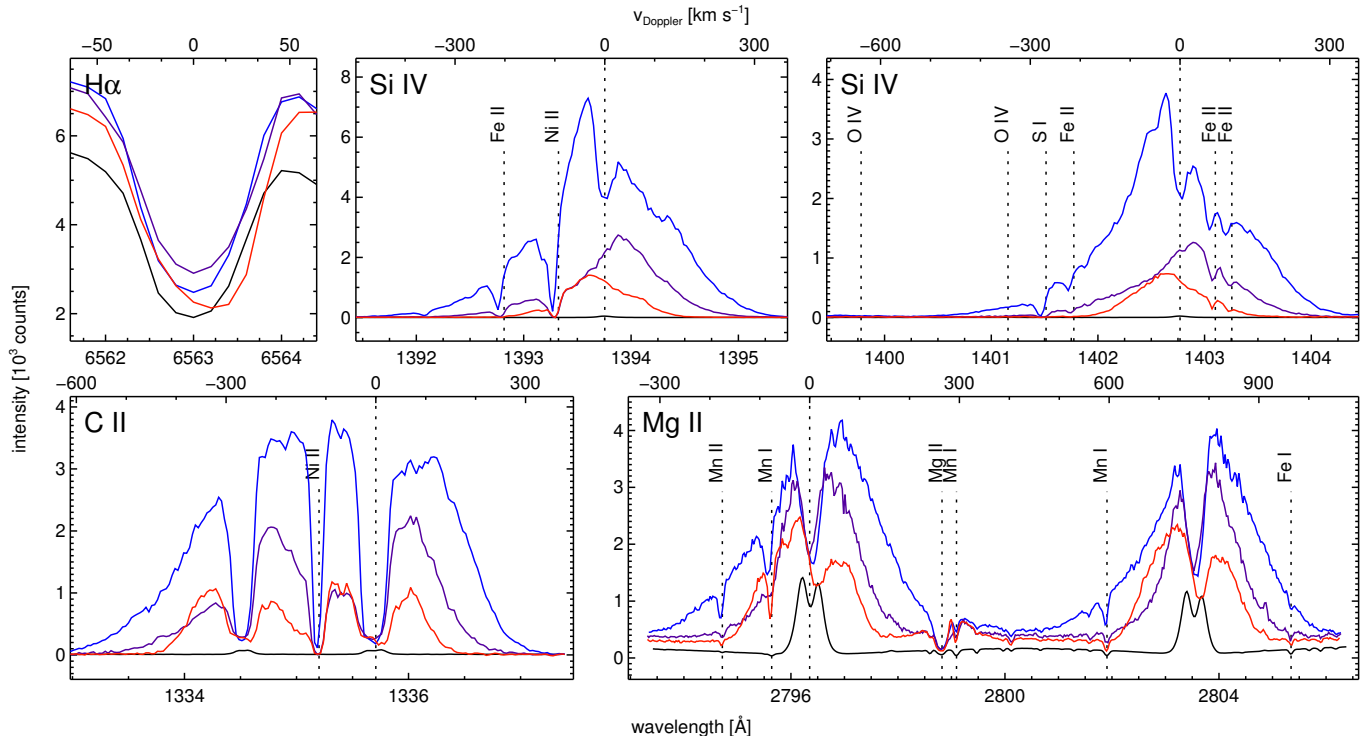


FIG. 16.— CRISP and IRIS spectra FAF-2 at the pixels marked in Fig. 14. Format as for Fig. 4.

#### 4.2. EB temperature estimation

The first conclusion from observing EBs in the IRIS lines is that EBs get very hot, especially in their tops. Such apparent heating to very high temperature in IBs was the main message of [Peter et al. \(2014\)](#) who wondered whether IBs are EBs or not. Our results show that both EBs and FAFs can produce IB signatures that suggest exceedingly hot events.

How hot precisely? [Peter et al. \(2014\)](#) cited the coronal-equilibrium presence temperature of 80,000 K for Si IV, but remarked that the actual ion distribution may be closer to LTE and peak at lower temperature.

Another way to estimate formation temperature is profile matching. In the idealized case of a convolution of thermal broadening with Gaussian non-thermal broadening and instrumental broadening the full-width at half maximum (FWHM) of the emergent profile from an optically thin homogeneous feature is  $\text{FWHM} = 1.67(\lambda/c) \sqrt{2kT/m + \xi^2 + \sigma^2}$  with  $m$  the atomic mass,  $\xi$  the non-thermal broadening, and  $\sigma$  the instrumental broadening. Figure 17 shows the possible combinations of thermal and non-thermal broadening that reproduce our observed halfwidth values. These range so wide that without precise knowledge of the non-thermal contribution this approach fails. In addition, our EBs are not truly thin nor homogeneous.

A better way to establish EB temperatures is profile matching with more sophisticated modeling. Modeling of H $\alpha$  profiles from EBs has been attempted by [Kitai \(1983\)](#), [Berlicki et al. \(2010\)](#), [Bello González et al. \(2013\)](#), and [Berlicki & Heinzel \(2014\)](#). They all applied ad-hoc perturbations of a static standard model to reproduce observed H $\alpha$  moustaches. Most defined the perturbation to not extend high, in order to avoid non-observed brightening of the H $\alpha$  core, but [Hong et al. \(2014\)](#) recognized

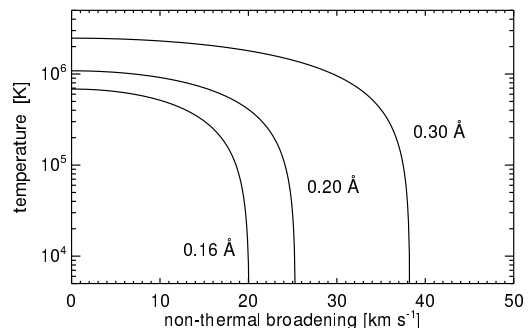


FIG. 17.— Gaussian profile fitting for Si IV 1403 Å. Each curve shows the combinations of temperature and non-thermal broadening that would produce the specified FWHM values bracketing our observations (0.16 Å for quiet Sun, the range 0.2–0.3 Å for EBs). The instrumental broadening was set at 4.1 km s<sup>−1</sup> following [De Pontieu et al. \(2014\)](#) and [Tian et al. \(2014\)](#).

that the core is actually formed in an overlying fibrillar canopy and should not be modeled as an EB property. They applied a two-cloud fitting model, one for the EB, the other for the canopy. These fitting exercises all claim that EBs represent temperature enhancements of the low standard-model chromosphere by at most a few thousand Kelvin, usually less. It seems highly unlikely that Si IV lines as displayed here can be obtained from any of them.

In addition to these trial-and-error fits, numerical EB simulations have been reported by [Chen et al. \(2001\)](#), [Isobe et al. \(2007\)](#) expanding on the serpentine emergence simulation of [Nozawa et al. \(1992\)](#), [Archontis & Hood \(2009\)](#), and most recently by [Nelson et al. \(2013b\)](#).

The most extensive simulation is the one by [Archontis & Hood \(2009\)](#) who specifically targeted EBs by setting up strong-field U-loop emergence. It also delivered temperature enhancements of order 1000 K. However, there

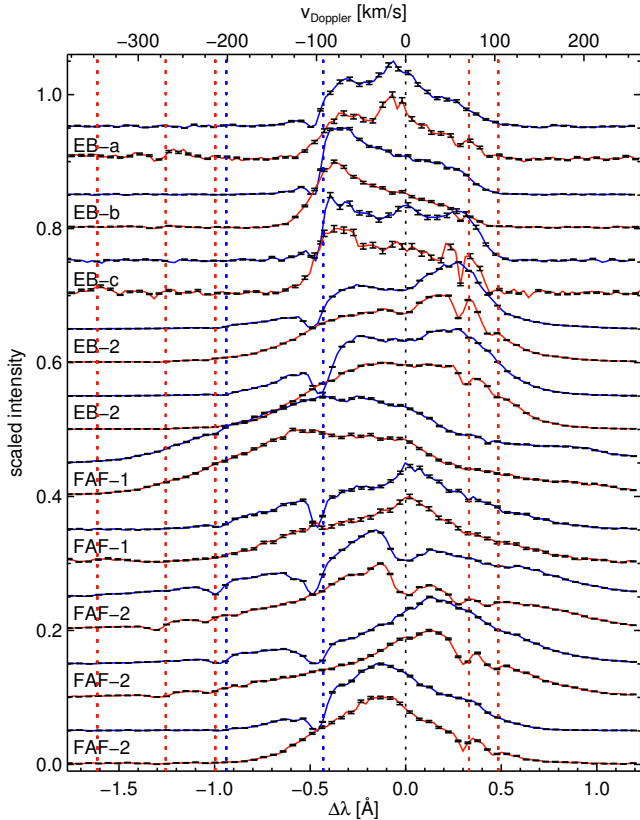


FIG. 18.— Stagger plot of normalized Si IV profiles to inspect commonality. For each feature that shows profile raggedness (labeled along the left side) selected Si IV 1394 Å profiles are shown in blue, the corresponding Si IV 1403 Å profiles in red, on a common wavelength offset scale with corresponding Dopplershifts along the top. Error bars for Poisson-noise estimates are overplotted in black for every other data point. The intensity range per line is 0.0–0.1, with offsets 0.05. Common dips in same-color profiles are due to absorbing blend lines. Common dips or humps per blue-red feature pair away from  $\Delta\lambda = 0.0$  indicate fine-structure mapping. Other fine structure is mostly measurement noise. The dashed lines, with corresponding color coding, specify rest wavelengths of major lines, from left to right: O IV 1401.16 Å (red, i.e., blend on Si IV 1403 Å), Si IV 1401.51 Å (red), Fe II 1401.77 Å (red), Fe II 1392.82 Å (blue, i.e., blend on Si IV 1394 Å), Ni II 1393.32 Å (blue), Si IV 1394 and 1403 Å (black, defining  $\Delta\lambda = 0$ ), Fe II 1403.10 Å (red), Fe II 1403.26 Å (red). was no proper accounting for radiation and no spectral synthesis of e.g., H $\alpha$ .

The most recent simulation, by Nelson et al. (2013b), did not set up an active-region emergence event but quiet-Sun magnetoconvection. If their reconnection event was an EB then EBs should appear all over the Sun, contrary to observation. The continuum brightening, core brightening (“line gap”) of Fe I 6303 Å and H $\alpha$  inner-wing brightening in their synthesized spectra (at top-down viewing, not slanted) suggests that they simulated a pseudo-EB. In any case, the heating was less than 1000 K.

The conclusion must therefore be that the fact that EBs show up in the IRIS lines contradicts all EB modeling efforts so far.

#### 4.3. Fine structure in IRIS profiles

There is fine-structure raggedness in the green and orange EB-2 profiles in Fig. 8, the EB-a, b and c profiles in Fig. 10, the orange and red profiles of FAF-1 in Fig. 13,

and the FAF-2 profiles in Fig. 16.

It can simply be measurement noise, especially at low count values (e.g., in the continua and overlapping wing part of Mg II and k in Fig. 4), but such noise contribution is smaller in bright line cores. The largest counts in the Si IV lines were reached for EB-2 (Fig. 8), but also these cores show ragged fine structure.

If the raggedness is not noise then it is either due to blends, which when present should re-occur at the same wavelength in different spatio-temporal samplings of a given line, or to profile mapping of fine structure in the event along the line of sight. In the latter case and in optically thick line formation, similar small-scale profile structure should appear at comparable optical depth sampling in different lines per pixel sampling, i.e., slightly further out from line center in the stronger component of a doublet. In optically thin line formation similar profile structure should occur at about the same Dopplershift in different lines per sampling.

Figure 18 details this choice for the two Si IV lines. In all cases their height ratio suggests optically thin or thinish line formation, so that the choice to explain raggedness is between noise, blends, and Doppler mapping of fine structure.

Most larger narrow dips re-occur at the same wavelength in different samplings of the same line (either blue or red) and are therefore blends. The major ones are identified by dashed lines with corresponding line colors. Most of these are blueshifted over about 10 km s<sup>−1</sup>. There are more blends, especially in the FAF-2 profiles as noted above.

The EB-a and EB-c profiles in Fig. 18 show the largest core raggedness, but also the largest raggedness in the adjacent continua and the largest noise (error bars in Fig. 18) because these cores reach only about 200 and 100 counts, respectively (Fig. 10). Indeed, the raggedness appears larger for the weaker red profiles and smaller in the brighter profiles from EB-b.

Finally, the somewhat larger-scale deviations from Gaussian profiles in the Si IV cores in Fig. 18 often show good similarity between the red and blue pair of profiles per sample. In view of the apparent optically-thin (or thinish) line formation of the Si IV lines we attribute such common fine structure to Dopplershift mapping of features along the line of sight.

For the EBs the presence of Dopplershift fine-structure fits the appearance of EBs in our SST H $\alpha$  movies as rapidly flickering flames and their bi-directional jet signatures. We surmise that rapid successive, intermittent reconnection of newly arriving opposite-polarity concentrations with varying flux content causes fast variations that eventually end up as fine structure in the resulting hot events.

For the FAFs the wide extent of the profile tails agree with the apparent observed filament extension speeds of 200 km s<sup>−1</sup>. The picture of thin fast-rising heating events also fits the morphology of the apparent lift-off of thin arcs and resulting bright arches in AIA 304, 171 and 193 Å, in particular after FAF-1.

#### 4.4. Nature of the hot events

EB-2 and the two FAFs produced spectra with IB hot-event signatures. EB-1 may have done so too, but its aftermath was not sampled by the IRIS slit. The weaker

EB-a, b and c did not. The upshot is that strong EBs can do so. Both FAFs certainly did.

The production of a hot event by upward progressing reconnection is not surprising. When in an EB two photospheric fluxtubes cancel against each other by reconnection, one may expect local temperature increase below a factor two because such fluxtubes tend to obey magnetostatic equipartition with their surroundings. This is indeed seen in the numerical MHD simulation of Archontis & Hood (2009). However, if the reconnection site then proceeds upward, the heating ratio increases because the magnetic energy diminishes less than the gas energy due to larger scale height. Much larger temperature increase may there be expected. In addition, the jet kicks are likely to cause Alfvénic wave generation and dissipation. Therefore, the observational indication that FAF reconnection occurs higher up than EB reconnection may explain why FAFs produce larger IBs and also million-Kelvin arches as FAF-1 did.

Various scenarios come to mind to produce hot gas with spectral blend superimposing by cooler and relatively stationary gas. The first is that this gas is simply undisturbed upper-photosphere or chromospheric canopy gas along the line of sight. We suggest that this is the case for the Mn I blends in the Mg II and k wings for the lines of sight to the feet of EB-1 and EB-2, and may likewise signify small event heights for EB-a, EB-b, and EB-c. Such blends were not present in FAF-1 which had the largest higher-atmosphere response of all our events, but for FAF-2 they were prominently present in the blue sampling in Fig. 16, superimposed on the widest of all our ultraviolet profiles, and still in the red sampling 17 min later. Assuming that these were from undisturbed “normal” gas along the line of sight implies that even FAF-2, which also showed filamentary extensions and AIA hot-diagnostic brightening, did not reach very high in its IRIS samplings.

We similarly speculate that the Fe II and Ni II blends on the Si IV and C II lines, which typically show blueshifts up to about  $10 \text{ km s}^{-1}$ , as also found by Peter et al. (2014), sample adjacent gas harboring upward propagating shocks as those in internetwork regions (e.g., Carlsson & Stein 1997; Leenaarts et al. 2007; Vecchio et al. 2009) and in dynamic fibrils near network and plage (e.g., Hansteen et al. 2006; De Pontieu et al. 2007; Heggland et al. 2007; Langangen et al. 2008).

Alternatively, an EB-like start-up FAF may kick cool photospheric gas up to large height where it can cause line-center dips and absorption blends, or these may originate in a post-bomb cooling cloud. However, such scenarios seem unlikely in view of the lack of large Doppler-shifts in the blend lines and central dips.

#### 4.5. *EB and FAF visibility in Mg II 2798 Å*

In our IRIS spectra the Mg II triplet lines appears with interesting behavior. Their emission profiles closely mimic the C II line shapes in EBs and in the initial EB-like stage of FAF-1, but not in the FAF spectra with stronger IB signatures. Strong presence of this line suggests a steep, deeply located temperature rise (Pereira et al. 2015). The marked appearances of Mg II 2798 Å in Figs. 4, 8 and 10 are indeed in good agreement with the C II and Si IV indications of high temperature already in

the lower-part samplings.

In Fig. 13 the line is very strongly present in the first sampling of FAF-1, almost as tall as h and k, so that the startup of FAF-1 resembled a low-atmosphere EB also in this respect. The later Mg II triplet profiles of FAF-1 in Fig. 13 are less extraordinary. In all FAF-2 samplings this line appeared in absorption (Fig. 16).

*EB and FAF visibility in H $\alpha$*  — H $\alpha$  is an extraordinary line, as is obvious from any solar H $\alpha$  filtergram. In EBs and FAFs it is also special. In EB-1 the H $\alpha$  top producing enhanced C II and Si IV emission is not seen in the first panel of Fig. 2, nor in the second panel. This suggests that hydrogen was already ionized in the upper part, as one would expect from Si IV visibility. However, in the other rows of Fig. 2 and also in Fig. 6 the H $\alpha$ -wing morphology resembles the IRIS 1330 Å slitjaw images. We believe that such hot response of H $\alpha$  stems from severe non-equilibrium recombination of hydrogen (Carlsson & Stein 2002; Leenaarts et al. 2007).

## 5. CONCLUSIONS

We have combined a comprehensive suite of solar observations. The relatively large field of view, unsurpassed image quality, and fast cadence of the H $\alpha$  imaging spectroscopy with the SST was indispensable to recognize both EBs and overlying fibrils from their spatial, temporal, and spectral behavior. The full-time full-disk monitoring by SDO served to separate EBs and FAFs in AIA 1700 and 1600 Å images and to inspect magnetic field evolution in HMI magnetograms. The IRIS slitjaw images, effectively providing high-cadence large-field images in the major IRIS lines, are an extremely valuable asset that previous solar ultraviolet spectrometers did not furnish. And last but not least, the spectra in the well-chosen set of IRIS lines emerge as varied “unveiled” EB diagnostics not hampered by overlying fibrils and offering rich signatures of what happens in the solar atmosphere at EB and FAF sites. They testify to Pannekoek’s dictum that “spectra constitute the astronomer’s treasure chest”.

We summarize our conclusions for EBs as follows:

1. the cores of H $\alpha$  and the Mg II h and k lines sample overlying chromospheric fibrils that are unaffected by the underlying EB. In these lines EBs are visible only well away from line center;
2. the IRIS Mg II triplet, C II, and Si IV lines sample the Ellerman bomb itself, often with optically-thin or near-thin formation of the Si IV cores;
3. these “unveiled” IRIS diagnostics indicate that the tops of Ellerman bombs become much hotter than all previous estimates in the literature;
4. they also give direct evidence of bi-directional jet behavior, with downdrafts of the lower parts and faster updrafts of the hotter upper parts;
5. subsequently, very hot post-bomb gas appears with wide and complex ultraviolet line profiles that suggest large Dopplershifts, possibly still from bi-directional jets, and much fine-scale structure. Even these remain a sub-canopy phenomenon.

FAFs seem to represent a comparable reconnection phenomenon, but breaking through or progressing along the



chromospheric canopy and causing much hotter structures that also become evident in million-Kelvin AIA diagnostics. The main difference with EBs seems that the reconnection is located or proceeds higher, but the blends and line-center-dips in the IRIS profiles from FAF-2 still suggest fairly deep formation.

For future EB modeling the ultraviolet line profiles from IRIS represent highly varied diagnostics furnishing such rich detail that modeling which succeeds in good reproduction is bound to be close to correct. If it does not succeed then such failure is bound to be instructive also. In this manner, EBs are likely to become the first solar reconnection phenomenon for which detailed modeling may be verified with certainty.

Since FAFs seem of larger interest with regards to upper-atmosphere mass and heat loading, verified EB modeling seems a worthwhile stepping stone to modeling FAFs properly. A good example in this direction is the recent study by Archontis & Hansteen (2014) of the formation of small flares from strong-field magnetoconvection producing serpentine emergence of the type proposed for EBs. Their resulting heating events and coronal jets are more substantial and located higher than EBs, but may well describe what we have called FAFs here.

Observationally, the next step is easier: catch EBs and FAFs in joint SST and IRIS (and of course SDO) ob-

serving campaigns targeting emerging active regions well away from disk center with a faster IRIS repeat cadence than in datasets 2 and 3. It would also be good to roll IRIS to put its slit along the projected vertical per target.

Our research has been partially funded by the Norwegian Research Council and by the European Research Council under the European Union's Seventh Framework Programme (FP7/2007-2013)/ERC grant agreement nr. 291058. B.D.P. was supported by NASA contract NNG09FA40C (IRIS). B.D.P., M.C., and L.R.v.d.V. have benefited from discussions at the International Space Science Institute (ISSI) meeting on "Heating of the magnetized chromosphere". IRIS is a NASA small explorer mission developed and operated by LMSAL with mission operations executed at NASA Ames Research Center and major contributions to downlink communications funded by the Norwegian Space Center through an ESA PRODEX contract. The SST is operated on the island of La Palma by the Institute for Solar Physics of Stockholm University in the Spanish Observatorio del Roque de los Muchachos of the Instituto de Astrofísica de Canarias. We thank T. Golding, T. Pereira, and H. Skogsrud for assistance with the SST observations and the referee for many useful suggestions.

## REFERENCES

- Archontis, V., & Hansteen, V. 2014, *ApJL*, 788, L2 [ADS](#)
- Archontis, V., & Hood, A. W. 2009, *A&A*, 508, 1469 [ADS](#)
- Bello González, N., Danilovic, S., & Kneer, F. 2013, *A&A*, 557, A102 [ADS](#)
- Berlicki, A., & Heinzel, P. 2014, *A&A*, 567, A110 [ADS](#)
- Berlicki, A., Heinzel, P., & Avrett, E. H. 2010, *MmSAI*, 81, 646 [ADS](#)
- Bernasconi, P. N., Rust, D. M., Georgoulis, M. K., & Labonte, B. J. 2002, *SoPh*, 209, 119 [ADS](#)
- Carlsson, M., & Stein, R. F. 1997, *ApJ*, 481, 500 [ADS](#)
- . 2002, *ApJ*, 572, 626 [ADS](#)
- Chen, P.-F., Fang, C., & Ding, M.-D. D. 2001, *Chin. J. A&A*, 1, 176 [ADS](#)
- de la Cruz Rodríguez, J. 2010, PhD thesis, Stockholm University [ADS](#)
- de la Cruz Rodríguez, J., Löfdahl, M. G., Sütterlin, P., Hillberg, T., & Rouppe van der Voort, L. 2015, *A&A*, 573, A40 [ADS](#)
- De Pontieu, B., Hansteen, V. H., Rouppe van der Voort, L., van Noort, M., & Carlsson, M. 2007, *ApJ*, 655, 624 [ADS](#)
- De Pontieu, B., Title, A. M., Lemen, J. R., et al. 2014, *SoPh*, 289, 2733 [ADS](#)
- Ellerman, F. 1917, *ApJ*, 46, 298 [ADS](#)
- Georgoulis, M. K., Rust, D. M., Bernasconi, P. N., & Schmieder, B. 2002, *ApJ*, 575, 506 [ADS](#)
- Hansteen, V. H., De Pontieu, B., Rouppe van der Voort, L., van Noort, M., & Carlsson, M. 2006, *ApJL*, 647, L73 [ADS](#)
- Heggland, L., De Pontieu, B., & Hansteen, V. H. 2007, *ApJ*, 666, 1277 [ADS](#)
- Henriques, V. M. J. 2012, *A&A*, 548, A114 [ADS](#)
- Hong, J., Ding, M. D., Li, Y., Fang, C., & Cao, W. 2014, *ApJ*, 792, 13 [ADS](#)
- Isobe, H., Tripathi, D., & Archontis, V. 2007, *ApJL*, 657, L53 [ADS](#)
- Kitai, R. 1983, *SoPh*, 87, 135 [ADS](#)
- Langangen, Ø., Carlsson, M., Rouppe van der Voort, L., Hansteen, V., & De Pontieu, B. 2008, *ApJ*, 673, 1194 [ADS](#)
- Leenaarts, J., Carlsson, M., Hansteen, V., & Rutten, R. J. 2007, *A&A*, 473, 625 [ADS](#)
- Leenaarts, J., Pereira, T. M. D., Carlsson, M., Uitenbroek, H., & De Pontieu, B. 2013a, *ApJ*, 772, 89 [ADS](#)
- . 2013b, *ApJ*, 772, 90 [ADS](#)
- Leenaarts, J., Rutten, R. J., Carlsson, M., & Uitenbroek, H. 2006a, *A&A*, 452, L15 [ADS](#)
- Leenaarts, J., Rutten, R. J., Sütterlin, P., Carlsson, M., & Uitenbroek, H. 2006b, *A&A*, 449, 1209 [ADS](#)
- Lemen, J. R., Title, A. M., Akin, D. J., et al. 2012, *SoPh*, 275, 17 [ADS](#)
- Lites, B. W., Shine, R. A., & Chipman, E. G. 1978, *ApJ*, 222, 333 [ADS](#)
- Matsumoto, T., Kitai, R., Shibata, K., et al. 2008, *PASJ*, 60, 95 [ADS](#)
- McMath, R. R., Mohler, O. C., & Dodson, H. W. 1960, *Proceedings of the National Academy of Science*, 46, 165 [ADS](#)
- Nelson, C. J., Doyle, J. G., Erdélyi, R., et al. 2013a, *SoPh*, 283, 307 [ADS](#)
- Nelson, C. J., Scullion, E. M., Doyle, J. G., Freij, N., & Erdélyi, R. 2015, *ApJ*, 798, 19 [ADS](#)
- Nelson, C. J., Shelyag, S., Mathioudakis, M., et al. 2013b, *ApJ*, 779, 125 [ADS](#)
- Nozawa, S., Shibata, K., Matsumoto, R., et al. 1992, *ApJS*, 78, 267 [ADS](#)
- Pariat, E., Aulanier, G., Schmieder, B., et al. 2004, *ApJ*, 614, 1099 [ADS](#)
- Pariat, E., Masson, S., & Aulanier, G. 2009, *ApJ*, 701, 1911 [ADS](#)
- Pereira, T. M. D., Carlsson, M., De Pontieu, B., & Hansteen, V. 2015, *ArXiv e-prints*, arXiv:1504.01733 [ADS](#)
- Pereira, T. M. D., Leenaarts, J., De Pontieu, B., Carlsson, M., & Uitenbroek, H. 2013, *ApJ*, 778, 143 [ADS](#)
- Peter, H., Tian, H., Curdt, W., et al. 2014, *Science*, 346, C315 [ADS](#)
- Rutten, R. J. 2003, *Radiative Transfer in Stellar Atmospheres* [ADS](#)
- Rutten, R. J., Vissers, G. J. M., Rouppe van der Voort, L. H. M., Sütterlin, P., & Vitas, N. 2013, *Journal of Physics Conference Series*, 440, 012007 [ADS](#)
- Scharmer, G. B., Bjelksjö, K., Korhonen, T. K., Lindberg, B., & Petterson, B. 2003, in *Society of Photo-Optical Instrumentation Engineers (SPIE) Conference Series*, Vol. 4853, *Innovative Telescopes and Instrumentation for Solar Astrophysics*, ed. S. L. Keil & S. V. Avakyan, 341–350 [ADS](#)
- Scharmer, G. B., Narayan, G., Hillberg, T., et al. 2008, *ApJL*, 689, L69 [ADS](#)

- Scherrer, P. H., Schou, J., Bush, R. I., et al. 2012, *SoPh*, 275, 207 [ADS](#)
- Shibata, K., Nakamura, T., Matsumoto, T., et al. 2007, *Science*, 318, 1591 [ADS](#)
- Shine, R. A., Title, A. M., Tarbell, T. D., et al. 1994, *ApJ*, 430, 413 [ADS](#)
- Tian, H., DeLuca, E. E., Cranmer, S. R., et al. 2014, *Science*, 346, A315
- van Noort, M., Rouppe van der Voort, L., & Löfdahl, M. G. 2005, *SoPh*, 228, 191 [ADS](#)
- Vecchio, A., Cauzzi, G., & Reardon, K. P. 2009, *A&A*, 494, 269 [ADS](#)
- Vissers, G., & Rouppe van der Voort, L. 2012, *ApJ*, 750, 22 [ADS](#)
- Vissers, G. J. M., Rouppe van der Voort, L. H. M., & Rutten, R. J. 2013, *ApJ*, 774, 32 [ADS](#) (Paper II)
- Watanabe, H., Vissers, G., Kitai, R., Rouppe van der Voort, L., & Rutten, R. J. 2011, *ApJ*, 736, 71 [ADS](#) (Paper I)
- Yang, H., Chae, J., Lim, E.-K., et al. 2013, *SoPh*, 288, 39 [ADS](#)